Naval Research Laboratory

Stennis Space Center, MS 39529-5004

NRL/MR/7320--12-9355

A Coupled Model System for Southeast Florida: Wave Model Validation Using Radar and In Situ Observations

Uriah M. Gravois

University of Florida
Gainesville, Florida

W. Erick Rogers
Tommy G. Jensen

Ocean Dynamics and Prediction Branch
Oceanography Division

February 24, 2012

REPORT DOCUMENTATION PAGE

Form Approved
OMB No. 0704-0188

1. REPORT DATE *(DD-MM-YYYY)*	**2. REPORT TYPE**	**3. DATES COVERED** *(From - To)*
24-02-2012	Memorandum Report	

4. TITLE AND SUBTITLE

A Coupled Model System for Southeast Florida: Wave Model Validation Using Radar and In Situ Observations

5a. CONTRACT NUMBER

5b. GRANT NUMBER

5c. PROGRAM ELEMENT NUMBER
0602435N

6. AUTHOR(S)

Uriah M. Gravois,* W. Erick Rogers, and Tommy G. Jensen

5d. PROJECT NUMBER

5e. TASK NUMBER

5f. WORK UNIT NUMBER
73-5097-22-5

7. PERFORMING ORGANIZATION NAME(S) AND ADDRESS(ES)

Naval Research Laboratory
Oceanography Division
Stennis Space Center, MS 39529-5004

8. PERFORMING ORGANIZATION REPORT NUMBER

NRL/MR/7320--12-9355

9. SPONSORING / MONITORING AGENCY NAME(S) AND ADDRESS(ES)

Office of Naval Research
One Liberty Center
875 North Randolph Street, Suite 1425
Arlington, VA 22203-1995

10. SPONSOR / MONITOR'S ACRONYM(S)
ONR

11. SPONSOR / MONITOR'S REPORT NUMBER(S)

12. DISTRIBUTION / AVAILABILITY STATEMENT

Approved for public release; distribution is unlimited.

13. SUPPLEMENTARY NOTES

*University of Florida, Gainesville, FL

14. ABSTRACT

This document describes the wave model validation efforts for a Florida Straits test case for the fully coupled Coastal Ocean/Atmosphere Mesoscale Prediction System (COAMPS) model during spring of 2005. The main focus of this work is validation of the waves portion of the COAMPS model; however, brief point analysis of winds and tides are also included. The "ground truth" for waves validation includes in situ data (ADCP and buoy) and high frequency Wellen Radar (WERA HF) data collected by the University of Miami. The wave height comparison to in situ data is generally good, though some wave events are overpredicted by the model. It is found that the accuracy of predictions of swell events is highly sensitive to the swell direction, and further that the range of directions from which swells are able to pass through islands and shoals to arrive at the in situ data region is highly sensitive to whether currents are included in the forcing. In the comparison to radar, the time series comparisons are mostly good, and the wave model with surface current forcing included shows a modestly improved accuracy compared to a model without currents. With regard to the ability of the models to capture the spatial variability evident in the radar, this depends on whether it is variability in the azimuthal or range position relative to the radar transmitter. In the context of the azimuthal position, it is suspected that the error statistics are unfortunately more reflective of the relative quality of the radar than the model skill. In the context of the range position, the situation is more favorable: this direction approximates the cross-shore direction, and variation of model and radar are in qualitative agreement in this case. The wave model with surface current forcing has higher correlation with the radar than does the model without currents. This not only supports arguments for operational coupled modeling systems, but is also indirect evidence of wave-current interaction in the radar observations.

15. SUBJECT TERMS

Wave model	NCOM	WERA	HF radar
SWAN	COAMPS	Wave-ocean coupling	

16. SECURITY CLASSIFICATION OF:			**17. LIMITATION OF ABSTRACT**	**18. NUMBER OF PAGES**	**19a. NAME OF RESPONSIBLE PERSON**
a. REPORT	**b. ABSTRACT**	**c. THIS PAGE**			W. Erick Rogers
Unclassified Unlimited	Unclassified Unlimited	Unclassified Unlimited	UU	45	**19b. TELEPHONE NUMBER** *(include area code)* 228-688-4727

This page intentionally left blank.

Contents

1 Introduction

This document describes work performed for a project to validate and transition a coupled wave-ocean forecasting system, led by R. Allard, NRL 7322. Selected material from this report will be incorporated into a Validation Test Report (VTR).

Within the general focus area of forecasting the battlespace environment, the two-way coupling between wave, ocean, and atmospheric models is a primary objective, as it is expected to offer a much more realistic representation of relevant physical processes than can be obtained through traditional one-way coupling. For example, though waves are intuitively understood to play a crucial role in the exchanges that occur across the air-water interface, in routine Navy operational forecasting outside the surf zone, the wave model outputs are generally disregarded in the computations of the atmospheric and ocean models. Further, even if the most appropriate theories and parameterizations to represent these physical linkages were clear (which they are certainly not), routine two-way coupling presents substantial technical challenges. Issues which may seem like trivial details to a scientist, such as efficiently transferring data between models running on different spatial grids and different time step sizes, can be very challenging. In the present case, the machinery to address these challenges is developed within the Earth System Modeling Framework (ESMF, see online at http://www.earthsystemmodeling.org/).

The atmospheric model in the present ESMF application is COAMPS (Coastal Ocean / Atmosphere Mesoscale Prediction System, Hodur 1997); the ocean model is NCOM (Navy Coastal Ocean Model, Martin 2000); and the wave model is SWAN (Simulating Waves Nearshore, Booij et al. 1999, SWAN 2010) [Since many different models have been adapted to run inside ESMF, and since in our case, most of the model interfaces occur via COAMPS, application of the coupled model system as used here is sometimes referred to as "running COAMPS"]. No other numerical models are used in the coupled system itself, though others are involved in the forcing, which will be discussed below.

Manuscript approved October 20, 2011.

Validation requires some form of ground truth, and in this instance, this is provided by a combination of in situ and radar data. The in situ sensors (ADCP and buoy) provide robust and reliable wave and tide data with the disadvantage that they provide limited spatial coverage. The WERA HF radar data have the advantage of wave measurement spatial coverage up to 55 km over a 120 degree field of view. However, with the increase in spatial coverage comes a decrease in confidence of the accuracy of the measurements. In order to make best use of the WERA HF data records used for this validation effort, substantial temporal filtering of outlier points and subsequent spatial and temporal averaging was required. The radar data were obtained in uncalibrated form and are calibrated here using comparisons between the in situ data and nearby radar values. The radar data are then divided into sectors for comparison to model waveheights collocated with the sectors. By subdividing the data into equal-area sectors, essentially organizing it by distance and azimuth angle, we are able to interpret the data in the context of data quality, which is expected to depend on distance and azimuth. For example, if data had instead been organized into rectangular shapes according to latitude and longitude, such interpretation would not have been possible. Though the main focus of this work is validation of the waves portion of the COAMPS model, brief point analysis of winds and tides are also included. Organization of this report is given in the Table of Contents.

2 Wave-ocean coupling methods

The VTR will contain more complete explanation of the wave-ocean coupling methods, but a qualitative description with references is provided here.

The ocean-to-wave coupling is straightforward insofar as it does not require any modifications of the respective model code. Water levels from the NCOM modify the water depth used in the wave model calculations. Surface currents are ingested by the wave model, which affect computations in a number of ways. First, they modify the effective wind speed (wind speed relative to a frame of reference moving with the currents). Second, the surface currents produce conservative (kinematic) effects on the wave field analogous to refraction and shoaling produced by depth variations. Third, horizontal shear in the currents can indirectly create non-conservative effects via the model source/sink terms (dynamics); for example, waves propagating from a region with zero currents into a regional of opposing currents will steepen, may break more frequently, and may even be blocked, resulting in persistent breaking at the blocking location. Fourth, Doppler shifting has implications for comparisons to data from fixed instruments.

Vertical structure of the currents is not used by the wave model. The coupled model system adopts the conventional paradigm as implemented in SWAN, which is to use the surface currents as representative of the entire vertical range in which waves act (in approximate terms, this is the typically the upper 200 m).

The wave-to-ocean coupling does require modification of the ocean model code. This coupling includes three separate mechanisms. First, the bottom drag is enhanced by the waves, in the tradition of Grant and Madsen (1979). This requires computation of variables describing the wave orbital velocity at the bottom.

Second, the radiation stress tensor is computed from the wave field, and the gradients of these tensors are used to calculate the local momentum surplus (or deficit) which is provided to the ocean model as a surface stress. This is sometimes referred to as the "classical method" for producing wave-induced circulation in a numerical model and is based on the work by Longuet-Higgins and Stewart (1962, 1964).

The third mechanism for wave-to-ocean coupling is via the Stokes drift. The Stokes drift profile is computed at each wave model grid point using an integration that considers spectral component wavelengths, spectral energy densities, and vertical position (see e.g. Tang et al. 2007). Momentum associated with the Stokes drift is carried in the wave field and is therefore not part of the mean Eulerian flow (e.g. Ardhuin et al. 2004, 2008). Therefore, the Stokes drift current (SDC) is *not* included in the prognostic momentum variables of the ocean model but *is* included in calculations requiring the observable mean flow, including a) advection of model fields, b) the continuity calculation (calculation of vertical velocity), c) the Coriolis term, d) calculation of bottom drag, and e) vertical mixing in the surface mixed layer.

3 Model Setup

Three wave model grids were used for this validation effort. WAVEWATCH III™ (Tolman 2009, "WW3") is run on the outermost grid (wave grid 1) with wind forcing from the Navy's Operational Global Atmospheric Prediction System (NOGAPS, Hogan and Rosmond 1991) archives and Digital Bathymetry Data Base (DBDB2) bathymetry. The resolution of wave grid 1 conveniently matches the wind fields in NOGAPS archives[1]. Another run is made with WW3 on wave grid 2 using boundary conditions generated from the wave grid 1. The wave grid 2 also employs DBDB2 bathymetry but is forced by COAMPS. The SWAN wave model is run on wave grid 3 fully coupled with Navy Coastal Ocean Model (NCOM) and COAMPS. The wave grid 3 is forced at the boundaries with WW3 grid 2 outputs. A summary of the three grids is given below, and plotted in Figure 1.

wave grid 1: WW3

- $\Delta x = \Delta y = 0.5° \approx 55$ km
- Longitude: x = -100° to -0.5° W (260° to 359.5° E), nx =200
- Latitude: y =17° to 59° N, ny =85
- no boundary forcing

wave grid 2: WW3

- $\Delta x = 4' \approx 6.5$ km
- $\Delta y = 4' \approx 7.4$ km
- Longitude: x = -90° to -72° W (270° to 288° E), nx =271
- Latitude: y =21.2° to 40° N, ny =283
- boundary forcing from grid 1

[1] The resolution also matches the global WW3 used by the Fleet Numerical Meteorology and Oceanography Center (FNMOC)

wave grid 2.5: SWAN (no interaction with the coupled model)

- Δx = 4′ ≈ 6.5 km
- Δy = 4′ ≈ 7.4 km
- Longitude: x = -90° to -72° W (270° to 288° E), nx =271
- Latitude: y =21.2° to 40° N, ny =283
- single-component boundary forcing

wave grid 3: SWAN

- Δx ≈ 0.01° = 1 km
- Δy ≈ 0.009° = 1 km
- Longitude: x = -80. 8 to -78.8° W (279.2° to 281.2° E), nx =201
- Latitude: y =23.6° to 27.2° N, ny =401
- boundary forcing from grid 2

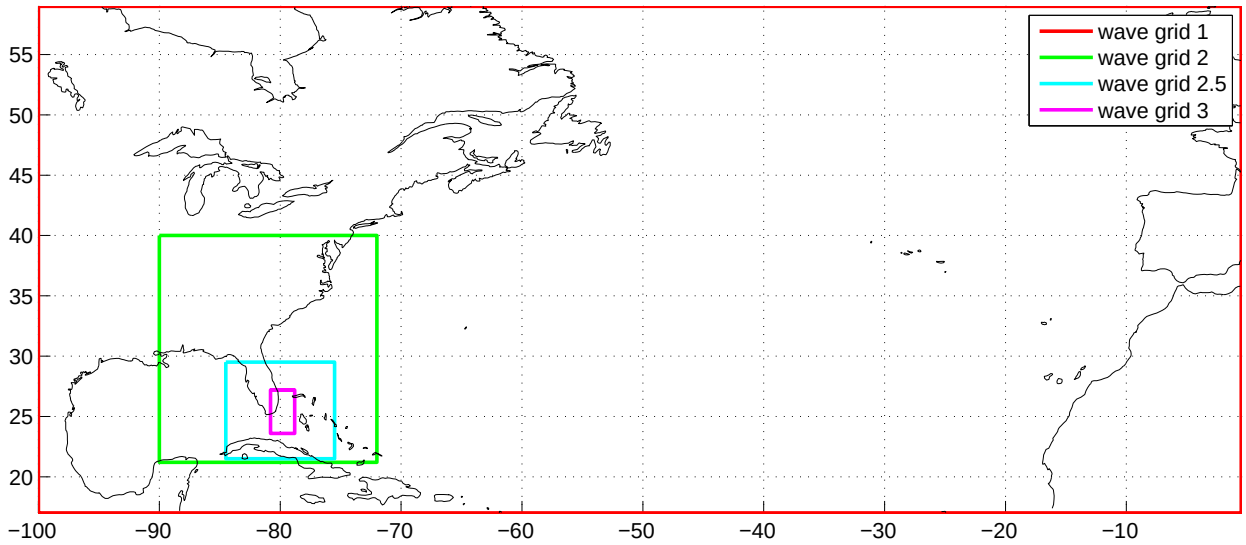

Figure 1: Geographic locations for the telescoping set of nested wave grids. Outer wave grids 1 and 2 are run on WW3 with NOGAPS and COAMPS wind forcing respectively. Inner wave grid 3 is run with SWAN as part of the fully coupled COAMPS model. Separate from the coupled model system, SWAN runs were made with grid 2.5 and grid 3 to investigate swell transmission into the in situ data area. This setup and results are discussed later.

To verify that wind forcing for grid 2 and boundary communications between grid 1 and grid 2 are set up properly, a qualitative check on the accuracy of the grid 2 wave model (WW3) is shown in Figure 2 ; model significant waveheight and peak period are compared with data from NOAA NDBC buoy 41010, 120 nm east of Cape Canaveral.

The general wave climate for the area is illustrated in Figure 3. This is for the NOAA NDBC St. Augustine buoy 41012 during all of 2009, so it does not correspond to the time period of the validation exercise.

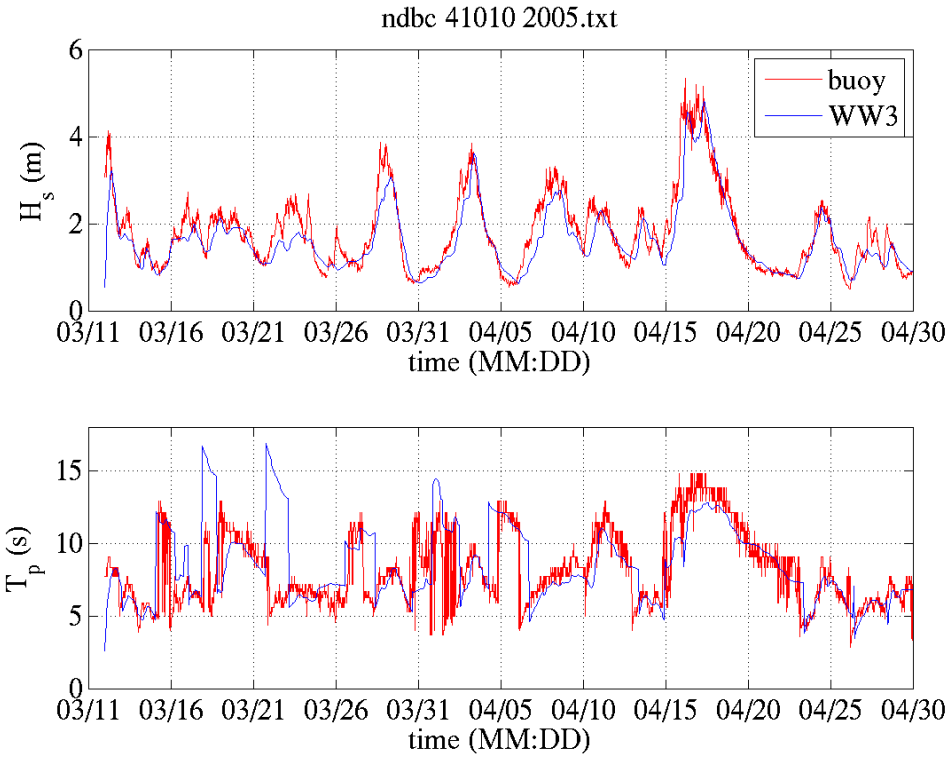

Figure 2: Qualitative check on accuracy of the grid 2 wave model.

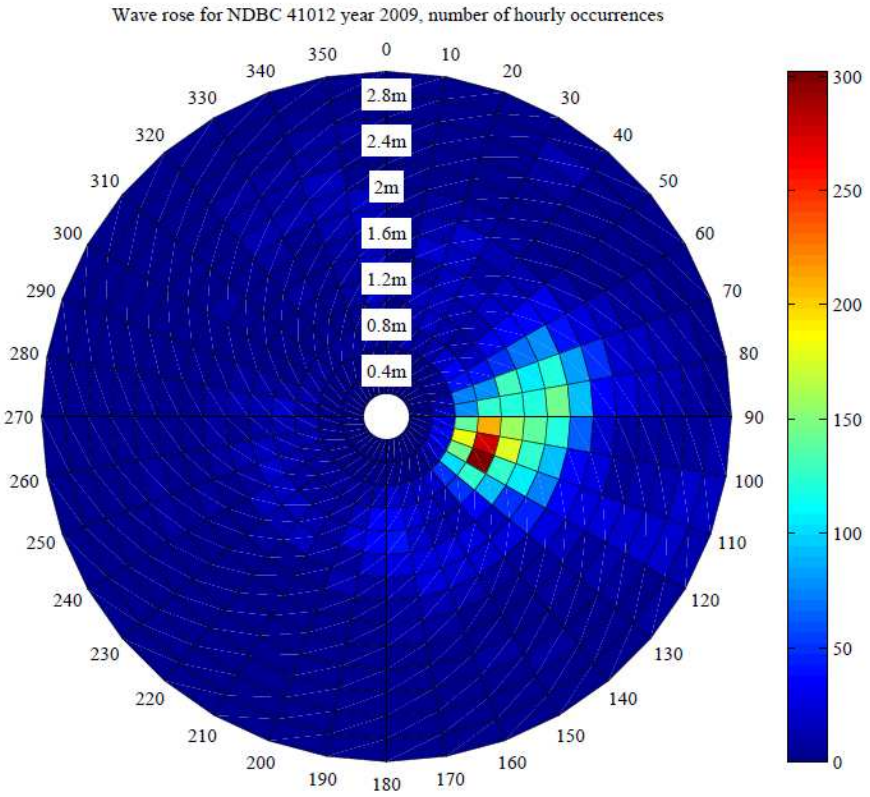

Figure 3 Wave rose for 41012. Number of occurrences by wave direction and waveheight.

Three simulations were performed for grid 3. First, a control model with full coupling between ocean and waves was run. This simulation employed the default bottom friction coefficient for ESMF SWAN (C_f =0.019 in the so-called JONSWAP formulation, see SWAN 2010). A case with ocean to wave coupling disabled and a fully coupled simulation with C_f increased by a factor of 3 were also run. The second simulation was run to quantify the impact of the coupling, and the third simulation was run to quantify sensitivity to bottom friction after it was observed that the model was overpredicting nearshore waveheights in some cases, as will be discussed below. The temporal overlap between the model simulations, the in situ data, and the radar data is presented graphically in Figure 4.

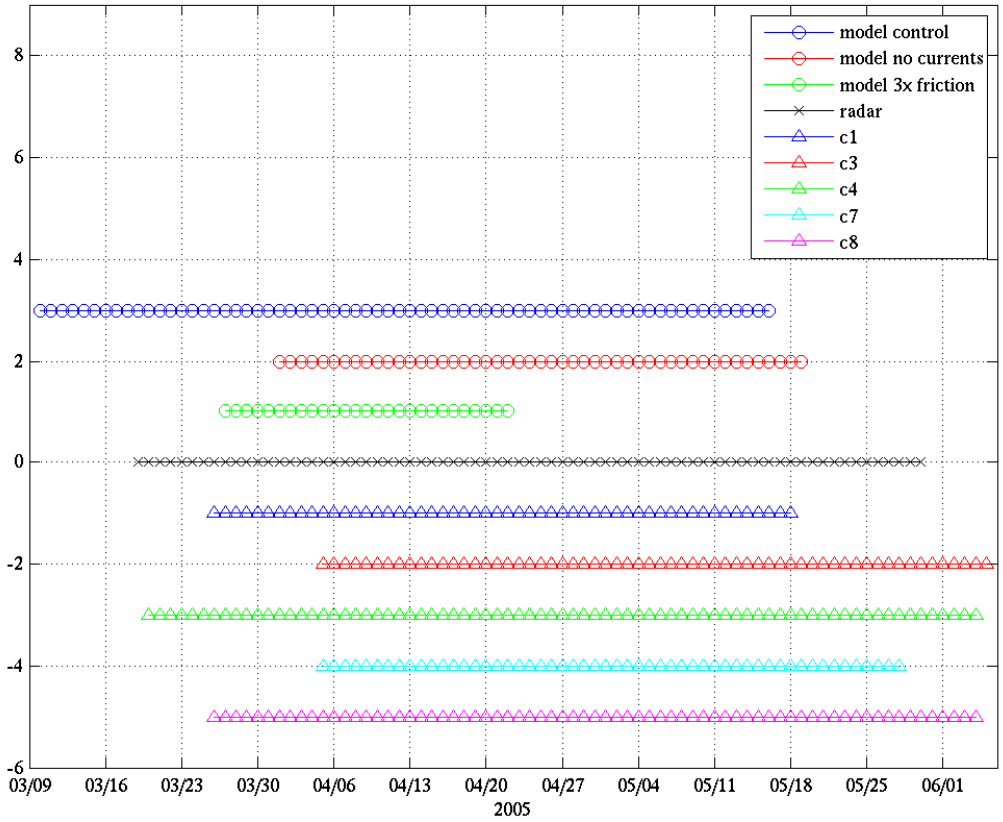

Figure 4. Temporal overlap of model simulations and observations. "Model control" is the fully coupled model with the default bottom friction coefficient for ESMF SWAN (C_f =0.019 in JONSWAP formulation), "no currents" is the simulation with ocean to wave coupling disabled, and "3× friction" is a fully coupled simulation with C_f increased by a factor of 3.

The WW3-to-SWAN nesting did encounter a technical problem, for which a workaround was implemented. Since the problem may be of interest to later users of the modeling system, it is briefly described now. The WW3 model creates boundary forcing files in ASCII format for SWAN using its point output feature. SWAN nesting is most straightforward if the nest files are provided in SWAN's spectral format, but SWAN does have a feature whereby it can read the WW3 ASCII files directly; that is the approached used here. These ASCII nesting files can be fairly large (this being true for both SWAN and WW3 files), e.g. with 129 boundary points, 529 dates, and a 25×36 spectral grid, the WW3 ASCII file size is 657 MB. However, the file size itself it not the primary problem. SWAN-to-SWAN nesting is fairly efficient, whereas WW3-to-SWAN nesting is not. This is most easily explained using an example. Take a case where the user has a nest file with many time records and requests that SWAN perform a stationary computation corresponding to the 100th time record in the nest file. With SWAN-to-SWAN nesting, SWAN will read the SWAN-format nest file in sequence until it gets to the record that it wants: record 1, record 2, record 3, …record 100; thus 100 records are read. With WW3-to-

SWAN nesting, SWAN will read the WW3-format nest file as records 1, 1, 2, 1, 2, 3, 1, 2, 3, 4, …100; thus 5050 records are read. The relative inefficiency increases geometrically, so the problem is much worse for long hindcasts. For nonstationary computations where the model start time corresponds to the first record of the nest file—as was true in our case—the simulation progresses quickly at first, but slows down exponentially. Though we identified these instructions in the SWAN code, we did not code a solution, since it was not determined why this odd approach was taken (i.e., would a correction just lead to more problems). Two workarounds were apparent, either to convert the spectra to SWAN format with a pre-processor, or to break the nest file into smaller increments (e.g. 12 hours). The latter approach was taken, since in an operational setting, the forcing fields would be available in small increments. In other words, in an operational setting, the workaround is already in place and no special action is needed; user intervention is only needed for long hindcasts.

4 Explanation of validation data

Several papers describing H-F radar measurements of waves were utilized during this study. A list of these papers, along with some other relevant references, is given here:

- Haus (2007): a study of fetch-limited growth; southeast Florida; December 2005.
- Haus et al. (2010): analysis of accuracy of waveheights from WERA; southeast Florida; calibration: YD 78-99 2005; Validation: YD 100-145 2005, in situ data used.
- Ramos et al. (2009): waveheights from several radars: North Carolina (SHOWEX, DUCK94) and Chesapeake Bay (COPE3)
- Shay et al. (2007): WERA surface currents; west Florida; August and September 2003.
- Shay et al. (2008) : primarily about surface currents, with some discussion of waves at several locations: west Florida, southeast Florida, and North Carolina,
- Voulgaris et al. (2008): wave measurements, including radar; southeast Florida radar, the "Mini-Waves Cal-Val experiment", YD 75-145 2005, discussion of calibration, waveheight and some directional spectra.
- Gurgel (1999), Wyatt et al. (1999, 2003), Caires (2000) : early European wave measurements with HF radar

The first period for the COAMPS model validation in the Florida Straits was from March 1 to May 18, 2005. During this late spring/ early summer time period, in-situ data were collected by the Rosential School of Marine and Atmospheric Sciences (RSMAS). These instruments were positioned outside of Biscayne Bay, Miami and recorded waves and currents at 5 point locations. These measurements were collected for an experiment named “mini waves”. A summary of the data types and deployment time periods are listed in Table 1. Latitude and longitude pairs for each instrument location are given. We found that the depths recorded at the actual instrument locations did not match those of the corresponding locations in the model: model depths were slightly too large on the Florida shelf. To remedy this, theoretical model locations were calculated west of the actual locations, where the model was shallower and was consistent with the measured depths at the in situ instruments. These locations are located inside the blue rectangle in the left panel of Figure 5 which is expanded in the right panel.

	start	end	Instrument	Actual Lat	Actual Lon	model lat	model lon	Depth (m)	1D spectra	2D stats	Tmean	Tpeak
C1	03/26/05	05/18/05	RDI ADCP	25.5006	-80.1101	25.5008	-80.1173	10	yes	yes	yes	yes
C3	04/05/05	06/05/05	TAB N	25.4991	-80.1025	25.4990	-80.1108	15	no	no	yes	yes
C4	03/20/05	06/04/05	SONTEK ADP	25.4987	-80.1087	25.4987	-80.1189	8.8	no	no	yes	no
C7	04/05/05	05/28/05	TAB S	25.4358	-80.1170	25.4359	-80.1251	15	no	no	yes	yes
C8	03/26/05	06/04/05	RDI ADCP	25.4705	-80.1134	25.4707	-80.1246	9	yes	yes	yes	yes

Table 1: RSMAS in situ data summary.

In addition to the in situ data, field measurements were also taken by a pair of high frequency Wellen Radars (WERA HF) operated by RSMAS. The two WERA HF radars located at Crandon Park (CDN 25°42.84'N, 80°9.06'W) on Key Biscayne and North Key Largo Hammocks Biological Preserve (NKL 25°14.46'N, 80°18.48'W) are separated by a distance of approximately 55 km. The spatial coverage of the wave height radar data extends roughly 50 km from the radar stations and spans over a 120 degree field of view centered on the bore-sight-angle. The bore-sight-angles were approximately 125° and 90° clockwise from North for the CDN and NKL stations respectively. The radar field grid spacing is regular at 1.2 km in both east-west and north-south corresponding to Δ longitude = 0.011940 and Δ latitude = 0.010799 which are equivalent if Δ longitude is multiplied by $\cos 25.26$ to account for Earth's curvature. The maximum range for radar wave measurements extends less in the radial direction compared to radar ocean surface current measurements. The WERA HF wave measurement areas are shown in the LHS of Figure 5.

Three Coastal-Marine Automated Network (CMAN) stations from the National Data Buoy Center (NDBC) and one National Ocean Service (NOS) tide stations lie within the wave grid 3 domain and were used for validation of the model winds and tides. These NOAA stations are shown on the left panel of Figure 5.

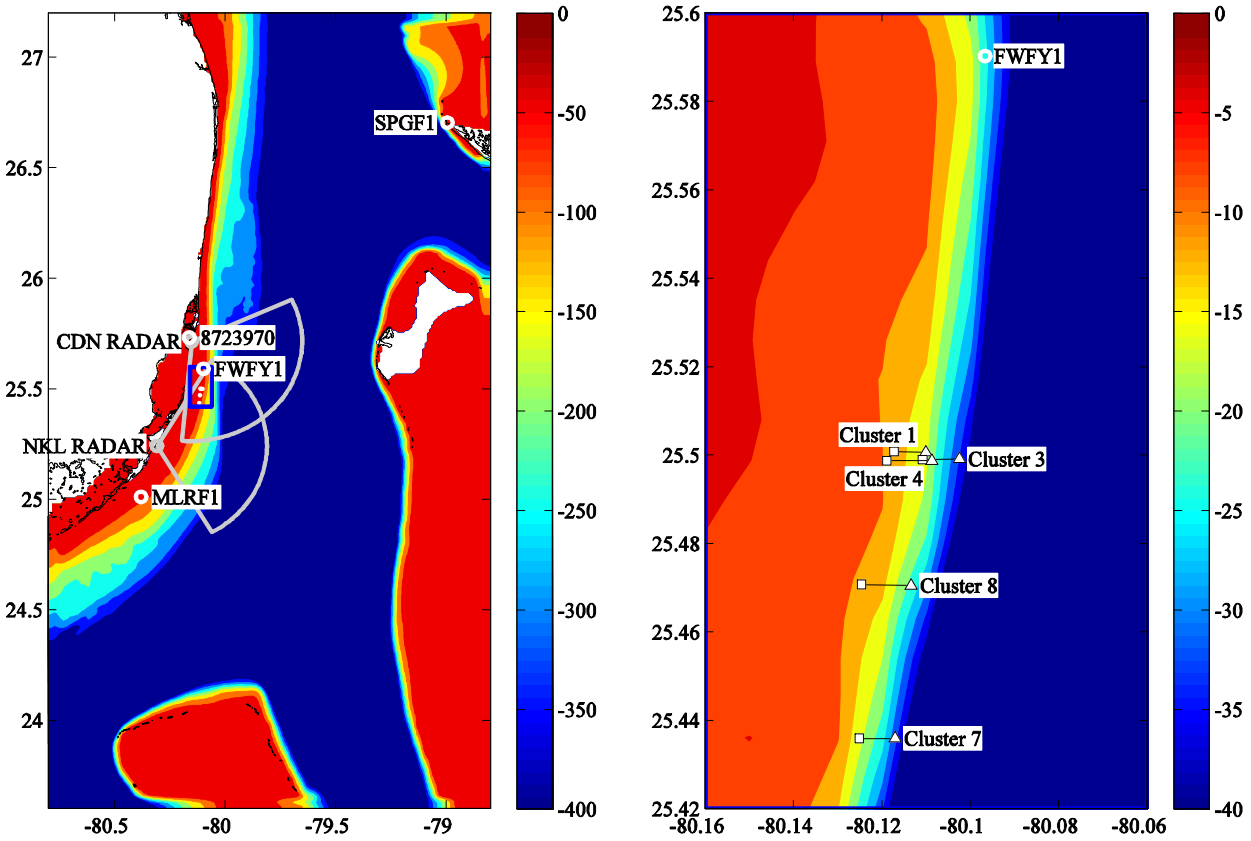

Figure 5 : The left panel is grid 3. The position of the two WERA HF stations CDN and NKL are shown with there respective swath wave sensing ranges. Included are the position of NDBC CMAN stations SPGF1, FWFY1, MLRF1 and NOS tide station 8723970. The Small blue box is expanded on the right side and showing the in situ locations detailed in Table 1 where the triangles represent the actual location and the squares the theoretical model locations.

5 Model wind and tide validation with NOAA coastal stations

The modeled tides matched a very well with the verified data at NOS tide station 8723970. However, prior to comparisons, both time series were demeaned to establish a consistent datum, i.e. the mean sea level of the two signals were treated as equal, even though this was not necessarily the case. The tide level comparisons are shown in Figure 6 and statistics are shown in Table 2. Comparison of the demeaned signals indicates reasonably good accuracy; the phase appears to be especially favorable.

The CMAN wind speeds were converted to 10 m elevation with a power law formula,

$$U_{10} = U_{instrument}\left[\frac{10}{z_{instrument}}\right]^{1/10},$$

and compared with the modeled winds. Visually, as seen in Figure 7-Figure 9, the wind speed and direction comparisons match well. The data statistics are presented in Table 2, the root-mean-square-error for the wind speed is near two and the correlation r – statistic vales are near 0.6 which is less good. Two things about the CMAN stations should be kept in mind: first, the data may have already been assimilated into the wind model and therefore these are not independent comparisons; second, these stations are mounted on land and drag and turbulence from land will effect the CMAN observations.

	bias	rmse	r - statistic
MLRF1 (wind speed)	-0.07	1.94	0.64
FWYF1 (wind speed)	0.08	2.00	0.57
SPGF1 (wind speed)	-0.28	2.32	0.62
8723970 (water level)	n/a	0.08	0.95

Table 2. Statistics of model vs. NOAA data. MLRF1, FWYF1, and SPGF1 represent NDBC CMAN stations (see Figure captions below), and 8723970 is a NOS tide station.

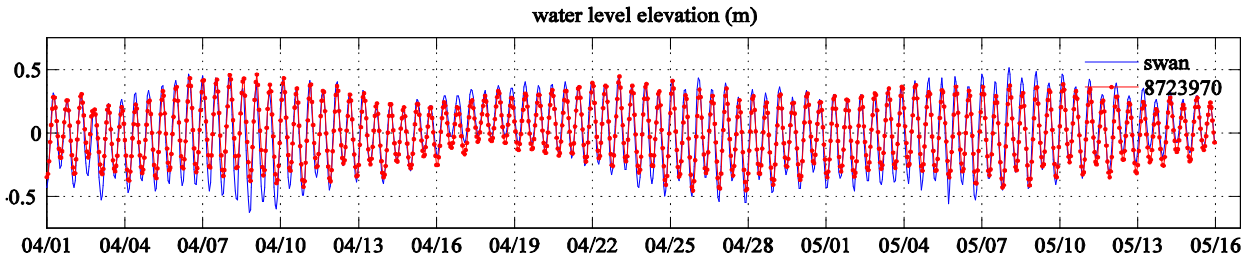

Figure 6 : Model simulated tide at Virginia Key NOS station 8723970 vs. verified hourly observations. Time series were demeaned so datum is MSL for the observation period.

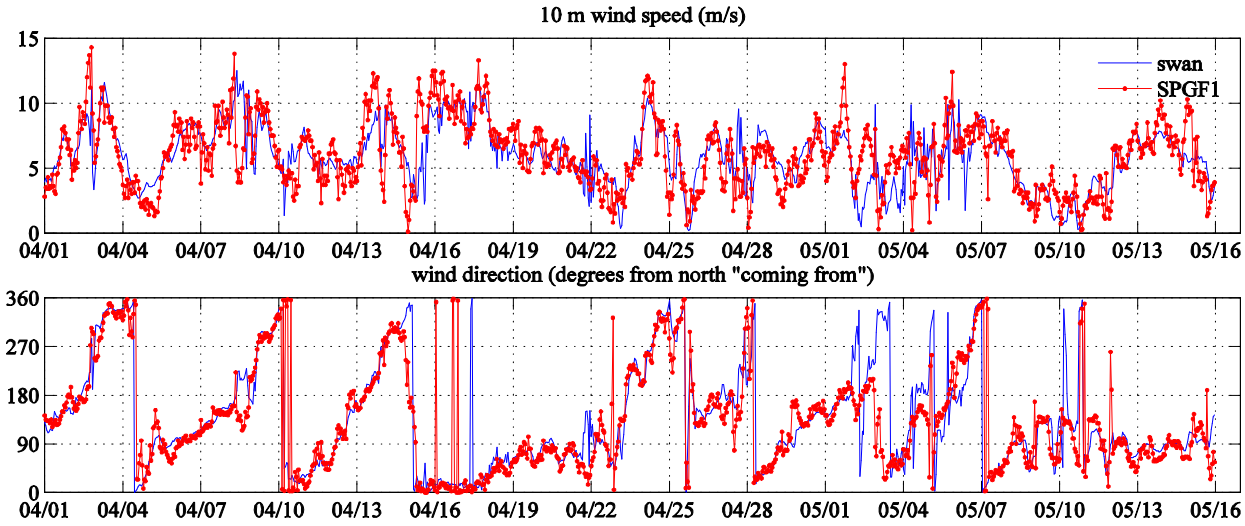

Figure 7 : Model simulated wind speed and direction at Settlement Point (SPGF1) CMAN station vs. hourly observations.

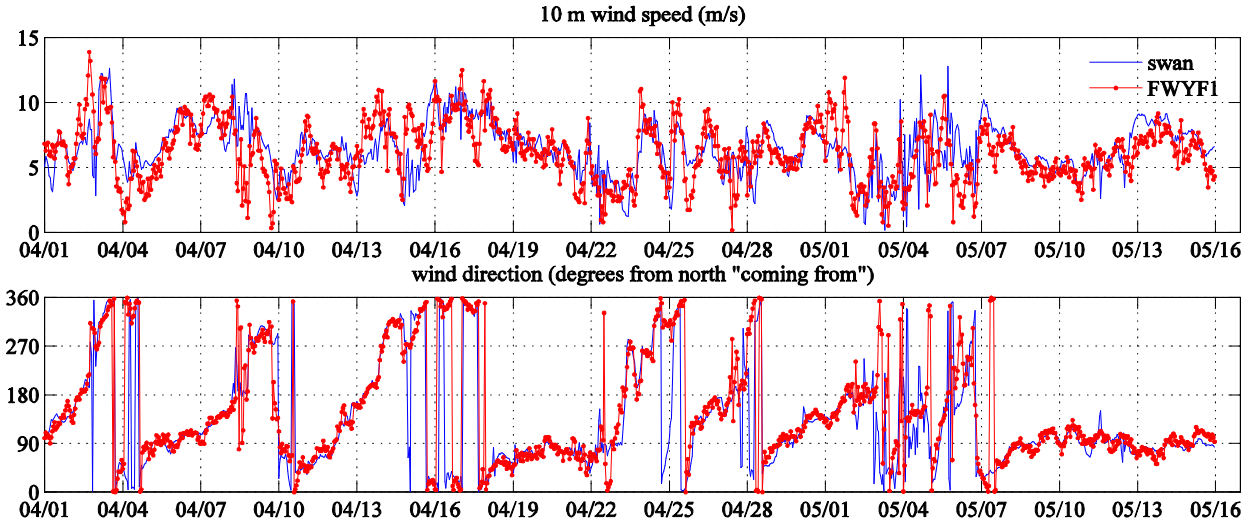

Figure 8: Model simulated wind speed and direction at Fowey Rocks (FWYF1) CMAN station vs. hourly observations.

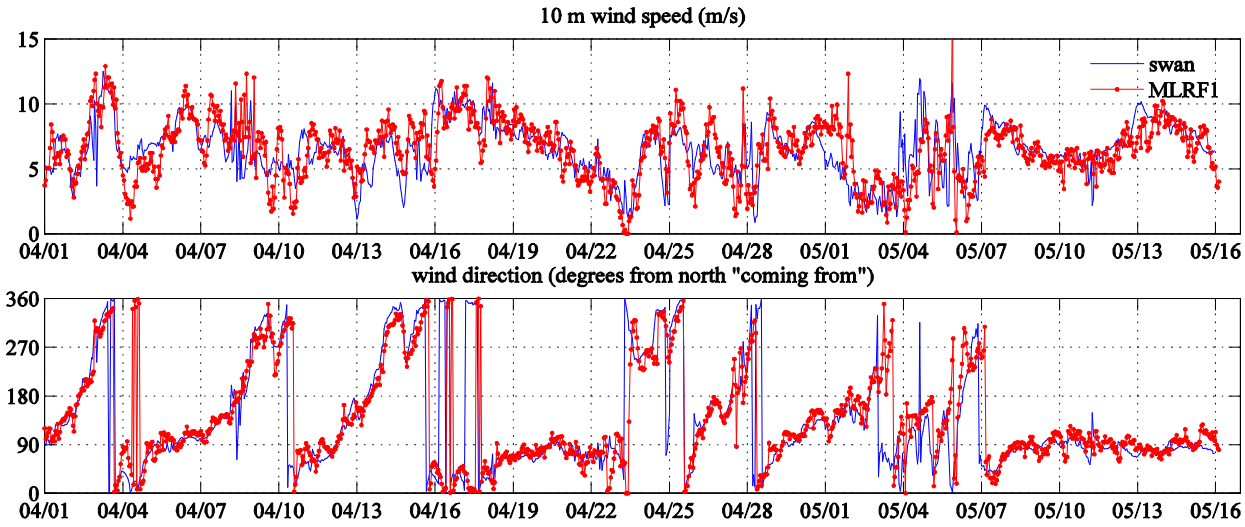

Figure 9 : Model simulated wind speed and direction at Molasses Reef (MLRF1) CMAN station vs. hourly observations.

6 Model validation against in situ measurements

Model wave height, direction and peak period from the theoretical model in situ locations were compared against the measured in situ data. Tabulated statistics for the wave height comparisons are shown in Table 3 and plots of the data are shown in Figure 10-Figure 14. (Statistics are for the period 01-Apr-2005 00:00:00 to 15-May-2005 23:00:00). Correlations were slightly better at the TAB stations which were in deeper water. Three notable events occur with waves approaching 1.5 m. The event starting around April 6 was captured by the model quite well. However, in the other two events occurring around April 3 and April 17 (the latter being the more significant event), the wave model over-predicts the waveheight. The two over-predicted events have mean wave directions from the NNE and there is a long period swell component.

The April 6 event that was modeled better did not have a long period swell component and the mean wave direction was from the east, meaning that this well-predicted energy was probably windsea generated inside the SWAN domain (grid 3).

The wave height over-prediction in the model for the two swell events (April 3 and 17) was not fully artificial; the WERA HF data also shows large waves for these events in the deeper water. This highlights the limitation of the point in situ measurements: they are not representative of offshore waves because the wave field is not homogeneous.

Perhaps the most credible explanation for the over-prediction is that the modeled waves at the in situ locations are sensitive to the wave angle at the model boundary. This was the conclusion of Rogers et al. (2007) who found for a SWAN hindcast of similar scale that even though the waveheight of their boundary forcing was quite accurate, the internal sheltering (blocking) by islands and other topographic features meant that the wave direction is also critically important: so much so, in fact that the wave height predictions at sheltered locations were sometimes severely biased due to errors in the directional distribution of the (otherwise accurate) boundary forcing.

The present simulation is also expected to be very sensitive to wave direction, again because of the amount of sheltering by islands and shoals. The mean wave directions reported by the in situ instruments indicate a measured mean wave direction slightly closer to north than in the model for the April 17 event. This may have had an impact on the model's over-prediction of the waves. In the real ocean, swells propagating toward the in situ data region from a northerly direction would have been turned into the coast by refraction, and therefore not reach those instruments. The same swell field propagating toward the radar would be in deeper water and therefore more likely to reach the radar (less likely to be trapped by refraction). In the model, the swells were propagating from a less steep angle (NNE) and so could penetrate into both regions (shallower in situ data region and deeper radar region).

To study this problem further, idealized simulations were performed on grid 2.5 (see Figure 1), which is similar to the domain of grid 3, except with the domain expanded somewhat to include the offshore islands and shoals that would potentially be blocking swells moving toward the observation locations. The simulations run with SWAN in "stationary mode" ($\frac{\partial}{\partial t} = 0$) and prescribed with idealized boundary forcing, with nearly all energy in one frequency/directional bin. A total of 48 simulations were run, each with a different swell direction (thus 7.5° intervals in direction between simulations)[2]. This was done both with and without currents included. Since the simulations were stationary, a single current field was needed; a representative "mean" NCOM field was selected for this. Figure 16 and Figure 16 show examples from two of the 48 simulations. The waveheight at the in situ data region was extracted from each simulation and the result was compared as shown in Figure 17. There are two very interesting features of this comparison: 1) there is a narrow range of preferential propagation directions for swell energy arriving at the in situ location, implying that a relatively small shift in wave directions at the swell source (Georgia Bight) could result in significant errors in wave energy at the in situ location (similar to Rogers et al. (2007) and 2) the direction from which swells are permitted to pass through the blocking topography is *highly* sensitive to whether the currents are included or not.

[2] A JONSWAP spectrum with 10 s peak period and significant wave height of 1.5 m is used for each simulation.

Error in the swell directions may be caused by errors in the wind forcing provided to WW3, e.g. a storm in the wrong location or winds blowing in the wrong direction.

There is a possible explanation other than the direction of the boundary forcing. The same type of error could result from error in the specification of the bathymetry (e.g. bathymetry too deep in parts of the domain). This was a point of specific concern in the COAMPS system, since NCOM does two things to the bathymetry: application of a minimum depth and smoothing. Normally, both modifications would be used in the SWAN computations, which is an unfortunately feature of the coupled system. In our case, we were able to prevent the use of the NCOM's minimum depth modification in SWAN, but the NCOM's smoothing was unfortunately still used in the SWAN runs.

It was determined in separate simulations that the overprediction is insensitive to the prescribed friction coefficient, implying that in the simulations, the modeled swell energy, prior to arriving at the in situ locations, propagates only a short distance over finite depth.

	bias	rmse	r - statistic
C1	0.09	0.23	0.69
C1-no currents	0.18	0.31	0.65
C3	0.08	0.23	0.74
C3-no currents	0.18	0.31	0.67
C4	0.22	0.32	0.68
C4-no currents	0.31	0.41	0.62
C7	0.04	0.19	0.80
C7-no currents	0.13	0.26	0.72
C8	0.13	0.23	0.73
C8-no currents	0.22	0.32	0.67

Table 3. Statistics of model vs. RSMAS in situ data. Comparisons include case with wave-ocean coupling disabled. The time period used is consistent between the two simulations. The C3 and C7 records start 4 days into this comparison period. Statistics are for the period 01-Apr-2005 00:00:00 to 15-May-2005 23:00:00.

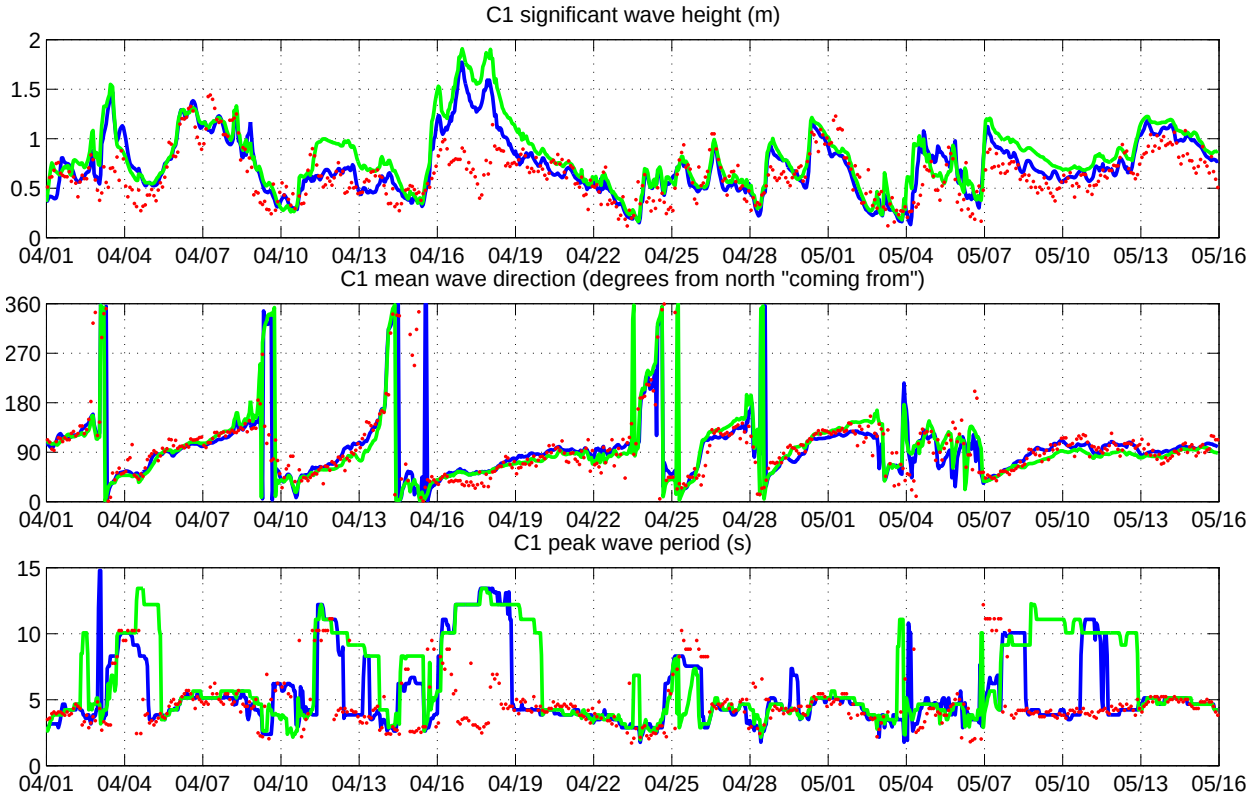

Figure 10 : Model vs. in situ data for the Cluster 1 ADCP in 10 m depth. The April 3 and April 17 events were swell events with energy generated outside of grid 3. The April 6 event was a windsea event with energy generated inside grid 3.

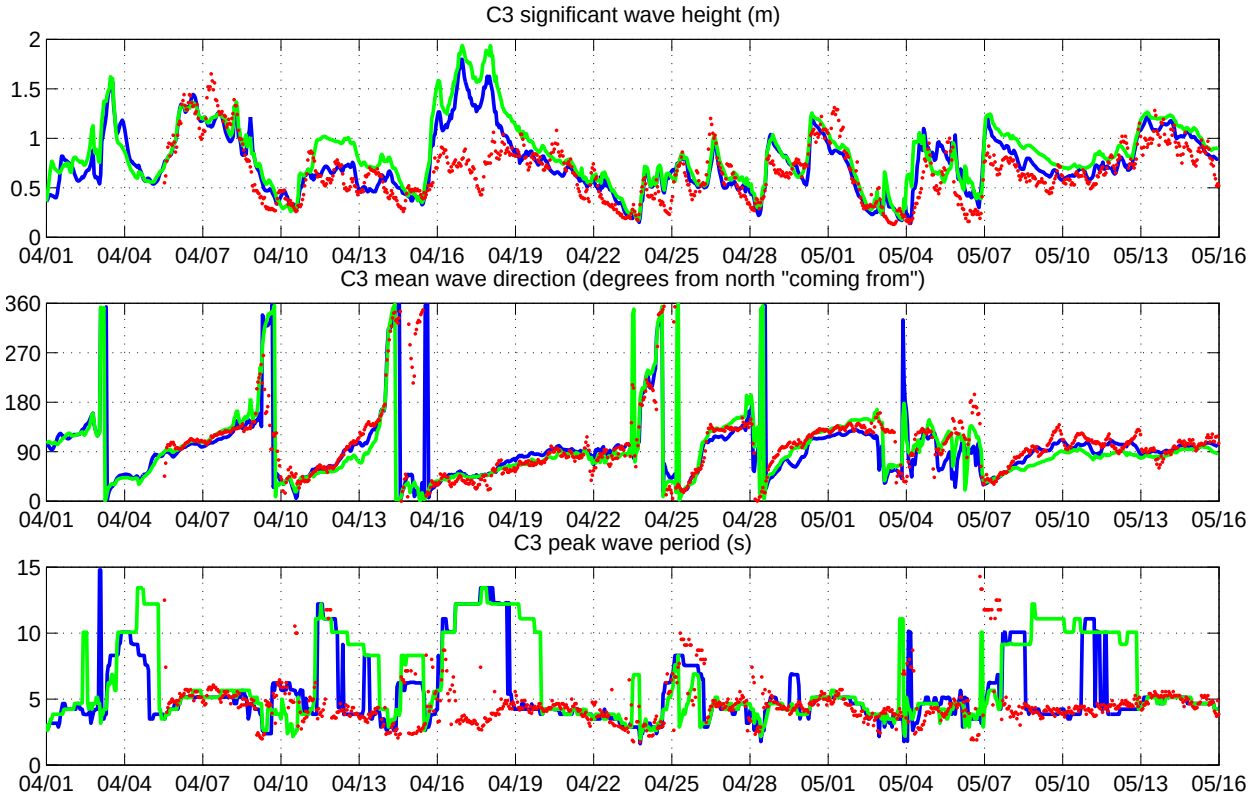

Figure 11 : Model vs. in situ data for the Cluster 3 TAB in 15 m depth.

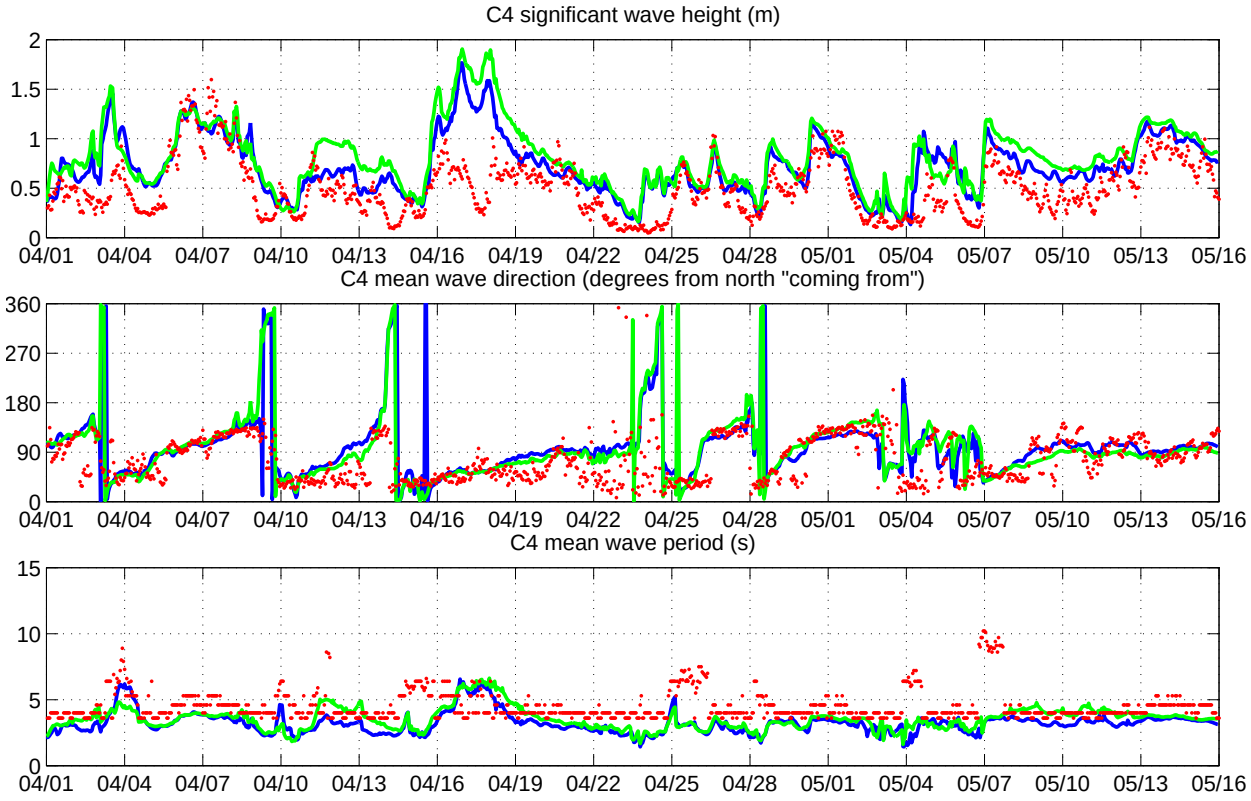

Figure 12 : Model vs. in situ data for the Cluster 4 ADP in 9 m depth.

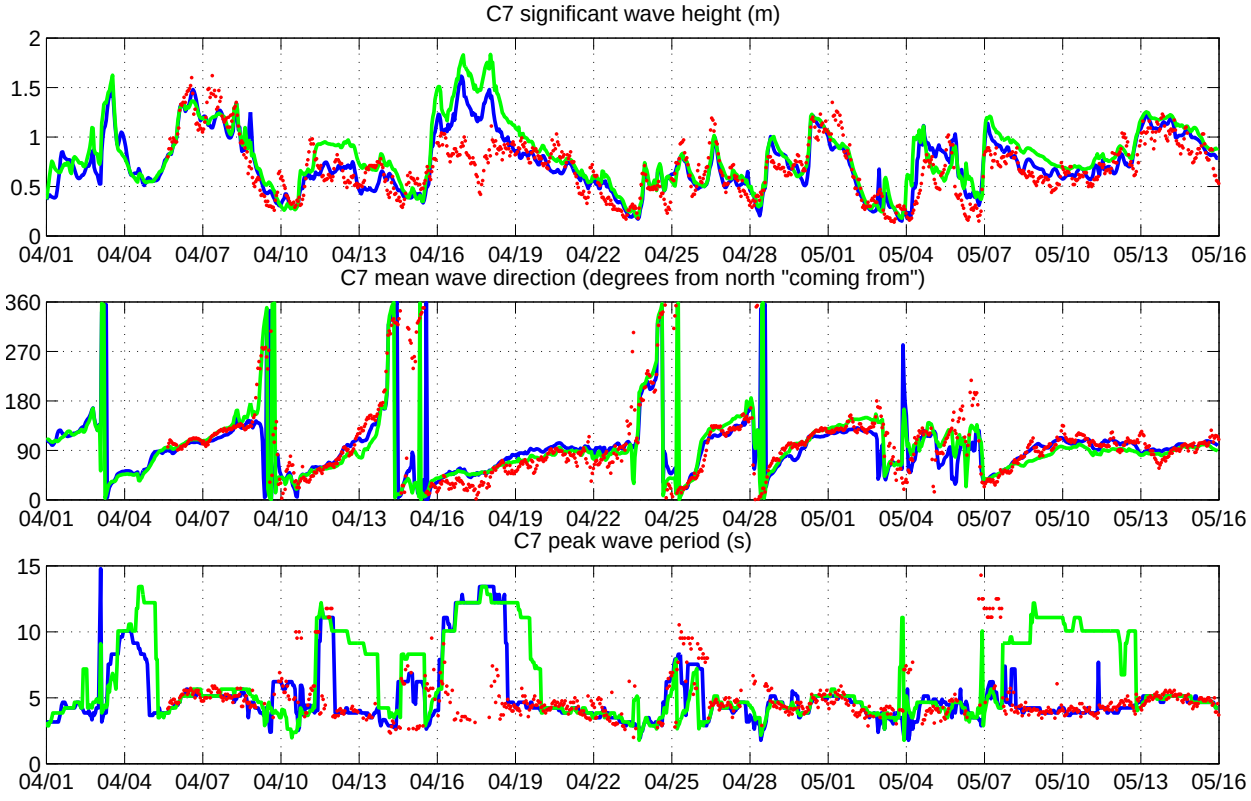

Figure 13 : Model vs. in situ data for the Cluster 7 TAB in 15 m depth.

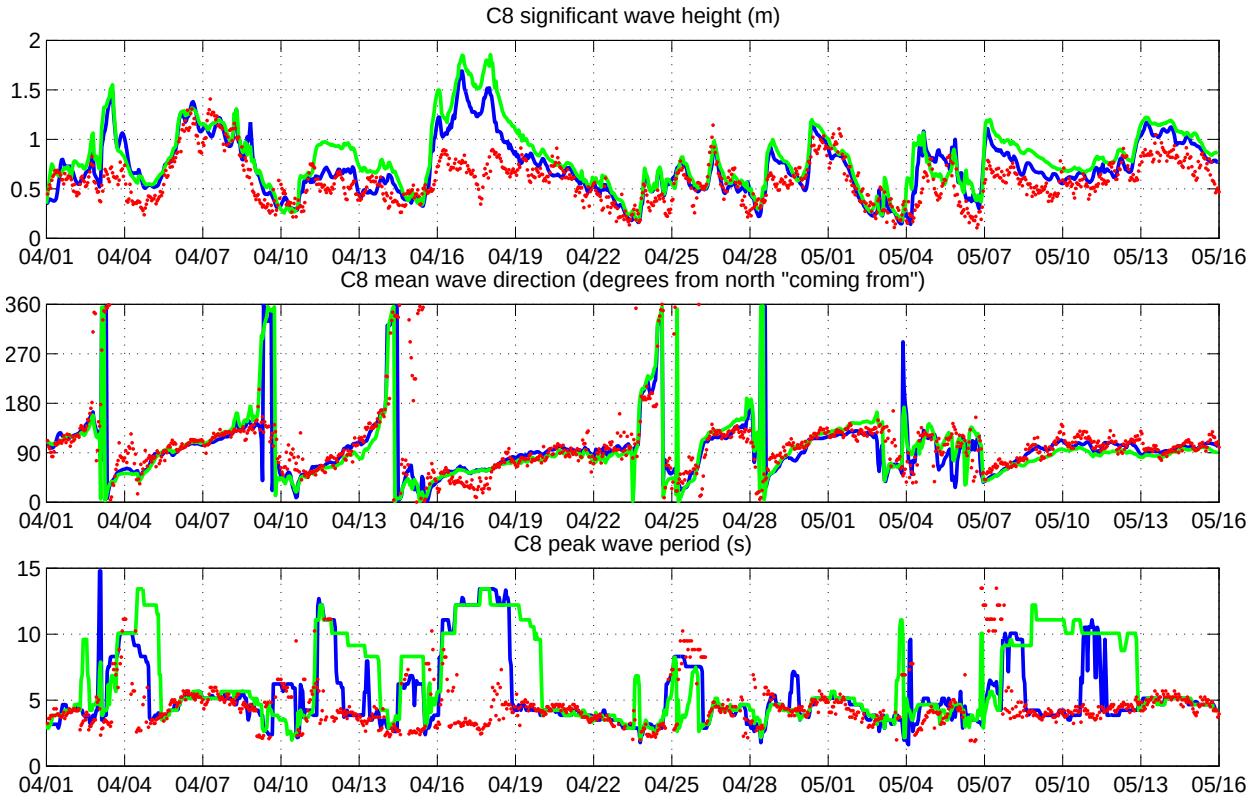

Figure 14 : Model vs. in situ data for the Cluster 8 ADCP in 9 m depth. Blue line=control model (currents ingested by SWAN), Green line=SWAN model without currents, Red line=in situ data.

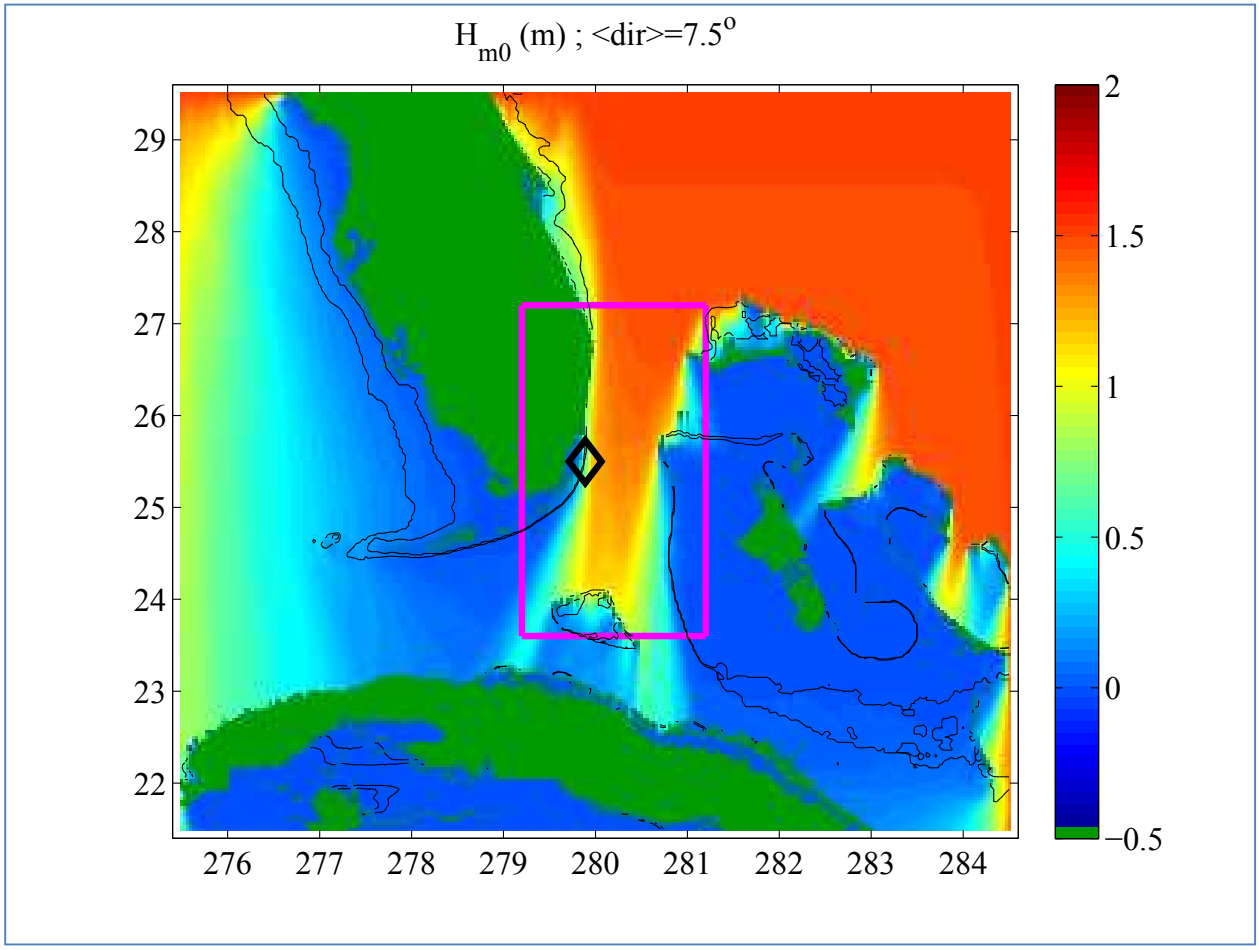

Figure 15. Idealized propagation in grid 2.5 with all incoming wave energy coming from boundaries with propagation direction in this case being θ=7.5° (from north-northeast). The magenta rectangle indicates grid 3. The black diamond indicates the in situ data location. Black lines are depth contours drawn at 10 and 20 m.

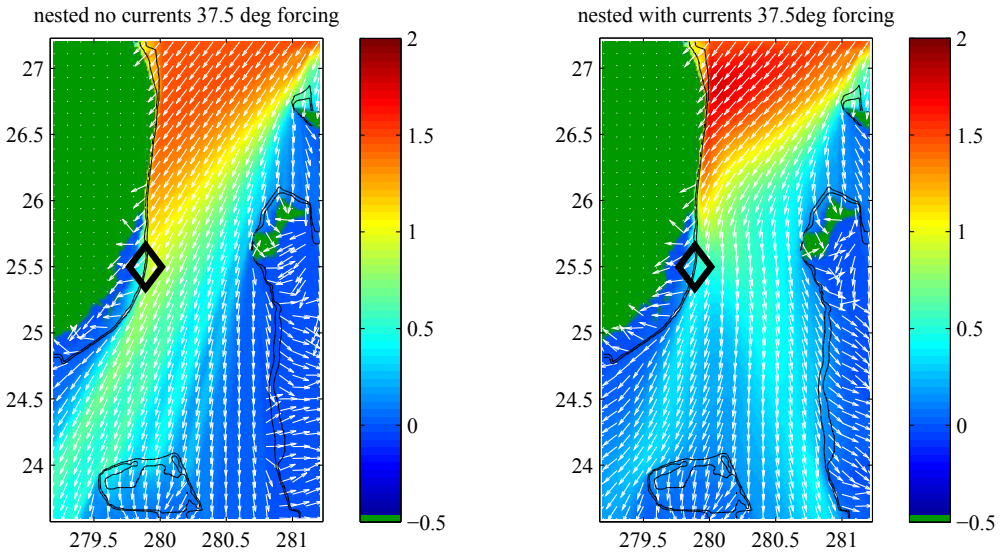

Figure 16. Idealized propagation in grid 3 with boundary conditions provided by grid 2.5, which in this case has all incoming wave energy with propagation direction θ=37.5° (from northeast). The black diamond indicates the in situ data location. Black lines are depth contours drawn at 0, 10 and 25 m. Arrows indicate mean wave direction.

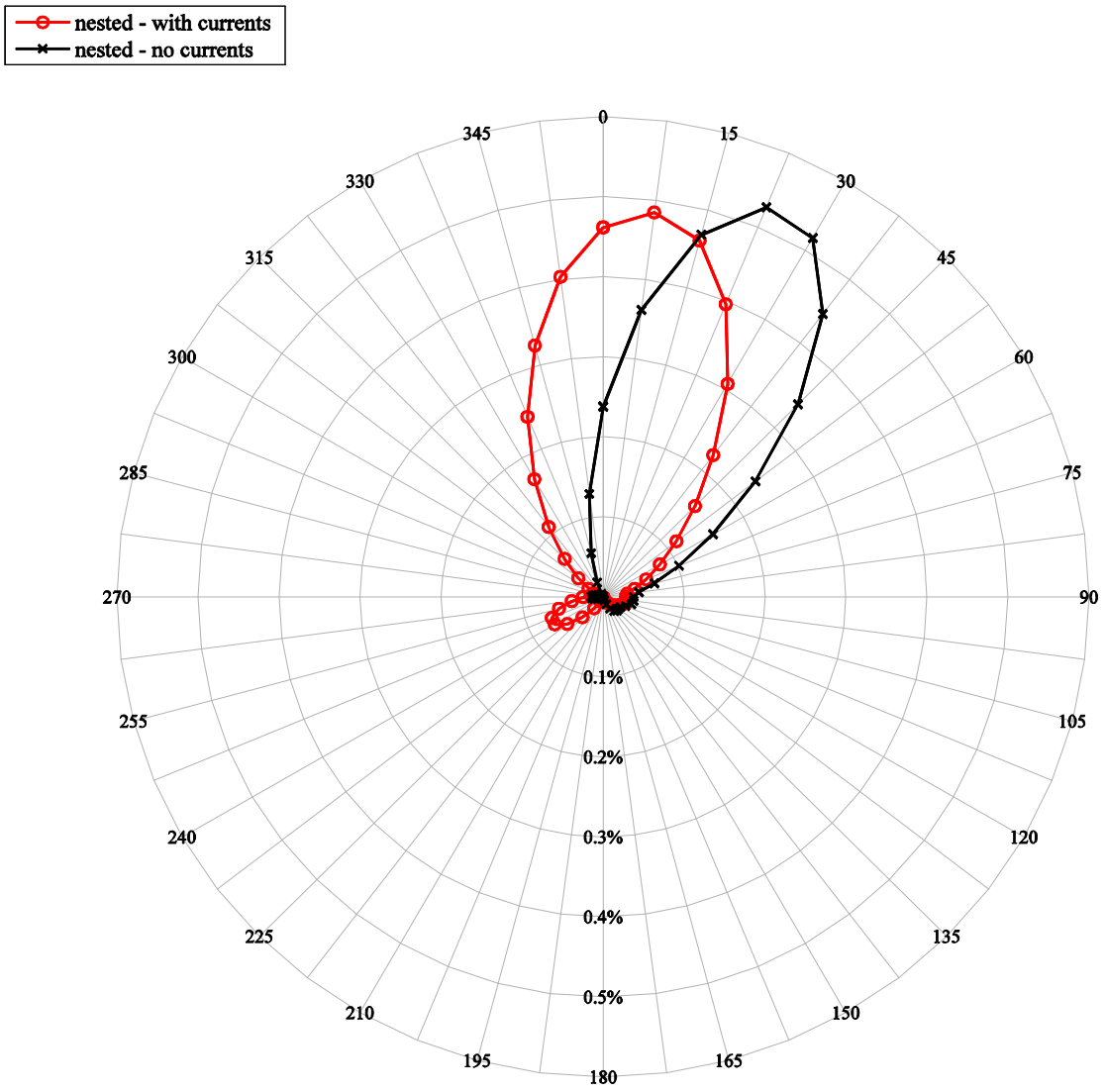

Figure 17 : Transmission percentage from offshore boundary forcing.

7 WERA HF data filtering

A major portion of this work was spent on processing the WERA HF wave measurements. The data was supplied by RSMAS in un-calibrated format with contaminated data points. An automated method to remove contaminated or outlier data was required prior to use in any validation.

The first step in the processing of the data was to pass each measurement cell through a temporal filtering algorithm to remove the outlier points. The details of this algorithm are as follows:

(1) Replace all zero values with "NaN" values.
(2) For a specific observation in time at WERA HF cell, consider 4 observations ahead and 4

observations behind in time and calculate the mean and standard deviation for these 8 observations.

(3) Determine if the central point is within 1 standard deviation of the mean.
(4) Determine if the standard deviation is between 0.01 and 0.15.
(5) Determine if 4 or more of the 8 observations are non-NaN values.
(6) Make a data mask which has NaN values for the central observation if it does not satisfy (3),(4) or (5) and a 1 otherwise.
(7) Loop through this routine for all measurement cells at all observations times.

This procedure was drastically sped up with parallelization across the spatial domain.

After the data was passed through the temporal filtering algorithm the data was then averaged over 1 hour period for all non-NaN data. After the data was filtered, the percent remaining of the data points relative to the original amount (Figure 18 and Figure 19) gives some indication of the spatial distribution of the initial data quality.

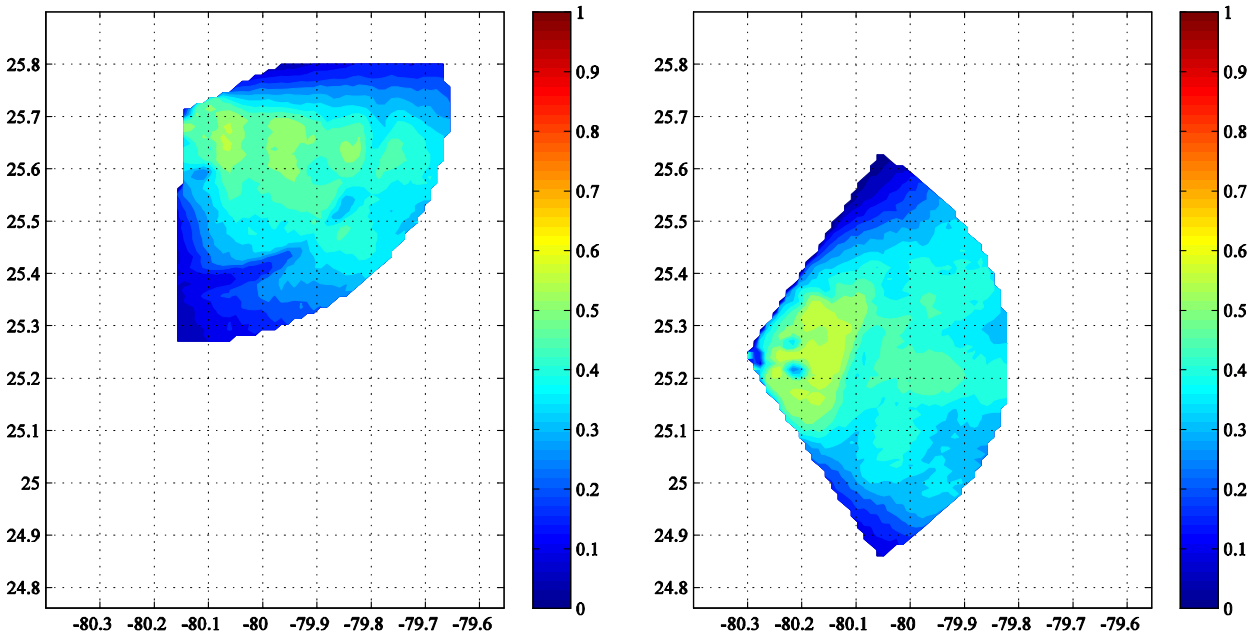

Figure 18: Percent of radar data remaining after outlier removal for 20 minute data.

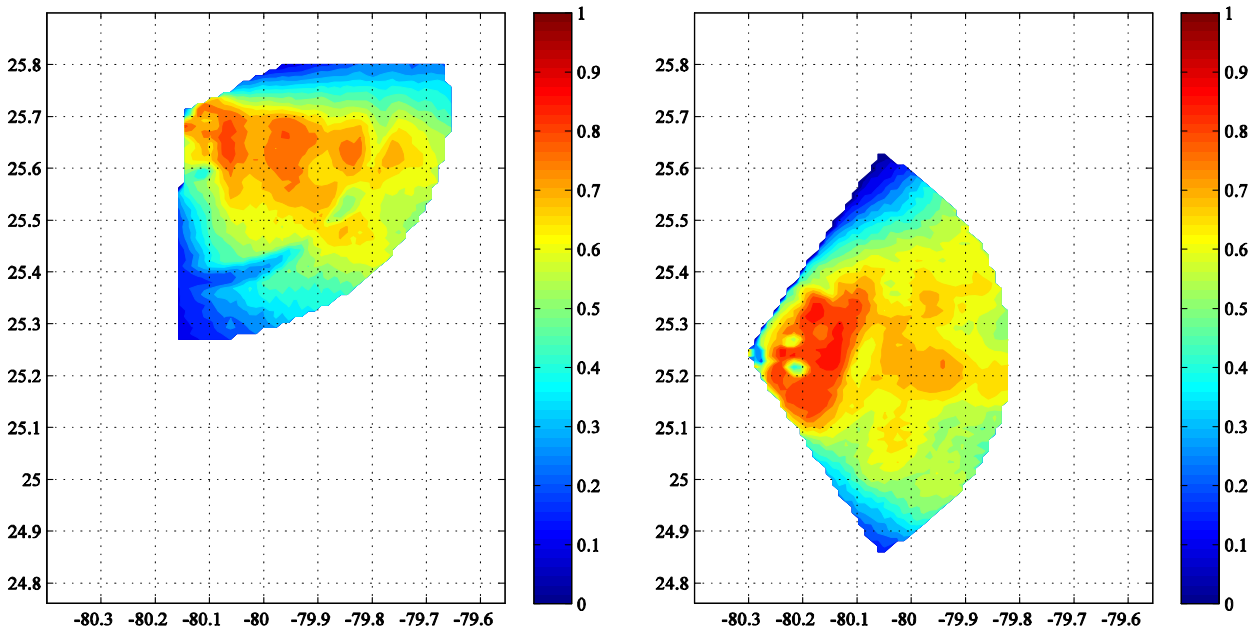

Figure 19: Percent of radar data remaining after summing to 1 hr.

8 WERA HF data calibration

Relevant papers referenced in Section 4 indicate that RSMAS preferred calibration of the radar data using a best correlated location that was far separated from and in much deeper water than the in situ data used for calibration. Our preference was to use radar data co-located with the in situ data, even if it meant using radar data of lesser quality.

The in situ data cluster number 7 was used for the radar calibration. 13 radar cells within 2.5 km of the in situ location were selected for use in the calibration. These points were available for both radars and the NaN mask was applied to both data sets for each hourly time observation. The non NaN points were averaged and used to perform robust linear regression (MATLAB) to find the best fit line in a scatter plot sense. A calibration ($slope \times radar\ value + offset$) was obtained for each radar and applied to all points. With the offset, in some rare cases radar points became negative and were reassigned to a value of zero. Plots of the robust least squares linear fits between the buoy and the radar are shown in Figure 20. The time period used for calibration is 05-Apr-2005 16:00:00 to 28-May-2005 08:00:00, which overlaps but is different from the time period for which the radar is compared to the models in Section 10 (01-Apr-2005 00:00:00 to 15-May-2005 23:00:00).

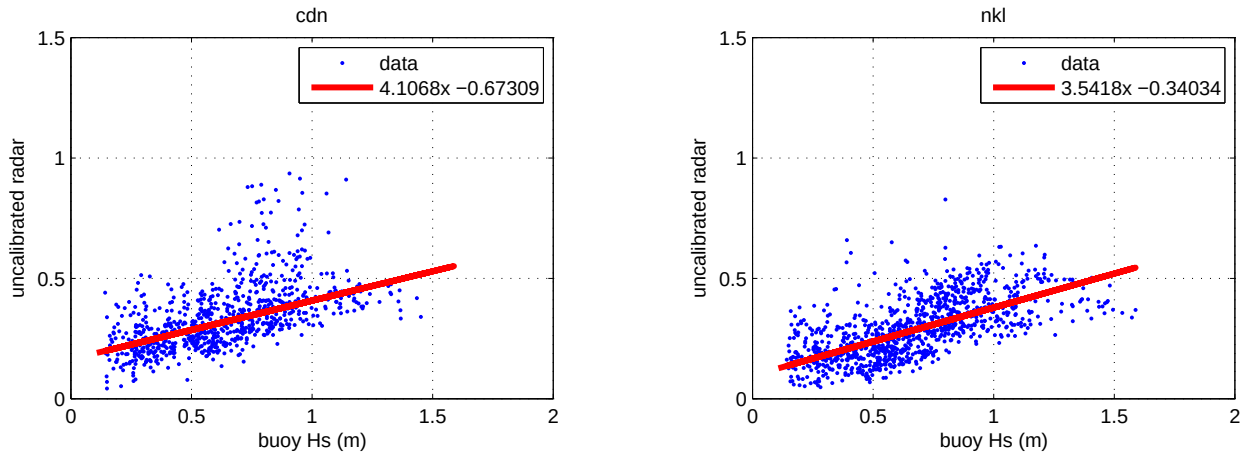

Figure 20 Plots of the robust least squares linear fits between the buoy and the radar.

9 WERA HF data sectoring

The data required more processing after the temporal filtering and a sector averaging scheme was devised. Here we divided the radar swath areas into 6 sectors of 20° and subdivided these sectors into 5 equal areas where the full radar swath is 120° and spans radially 50 km with 1.2 km spacing between points. Hence there are 30 sectors for each radar with approximately 50 points in each sector. For dividing the radar sectors, a great circle formulation was used to calculate the distance between the radar station and the cell in the return field:

$$\vec{\imath} = \cos(lat) * \cos(lon)$$

$$\vec{\jmath} = \cos(lat) * \sin(lon)$$

$$\vec{k} = \sin(lat)$$

$$km = \cos^{-1} \frac{\vec{\imath_1} \cdot \vec{\imath_2} + \vec{\jmath_1} \cdot \vec{\jmath_2} + \vec{k_1} \cdot \vec{k_2}}{360} * 40003.2$$

An arc-tangent equation was used to calculate the angle. These were sorted based on the criteria described above. The indices for the sectors are given by A-F for CDN and G-L for NKL with each having 5 areas, 1 through 5, increasing with distance from the center. These sectors are given in Figure 21 and Figure 22.

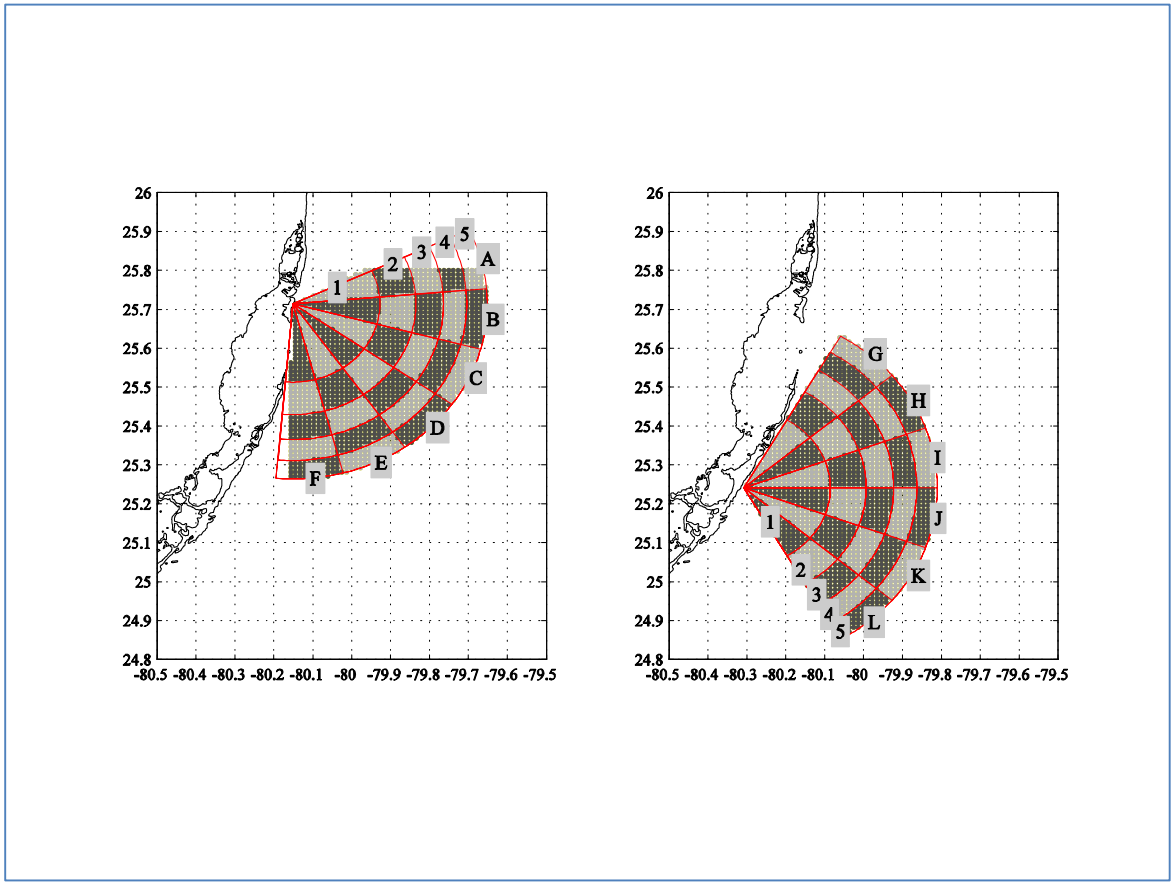

Figure 21. Radar sectors.

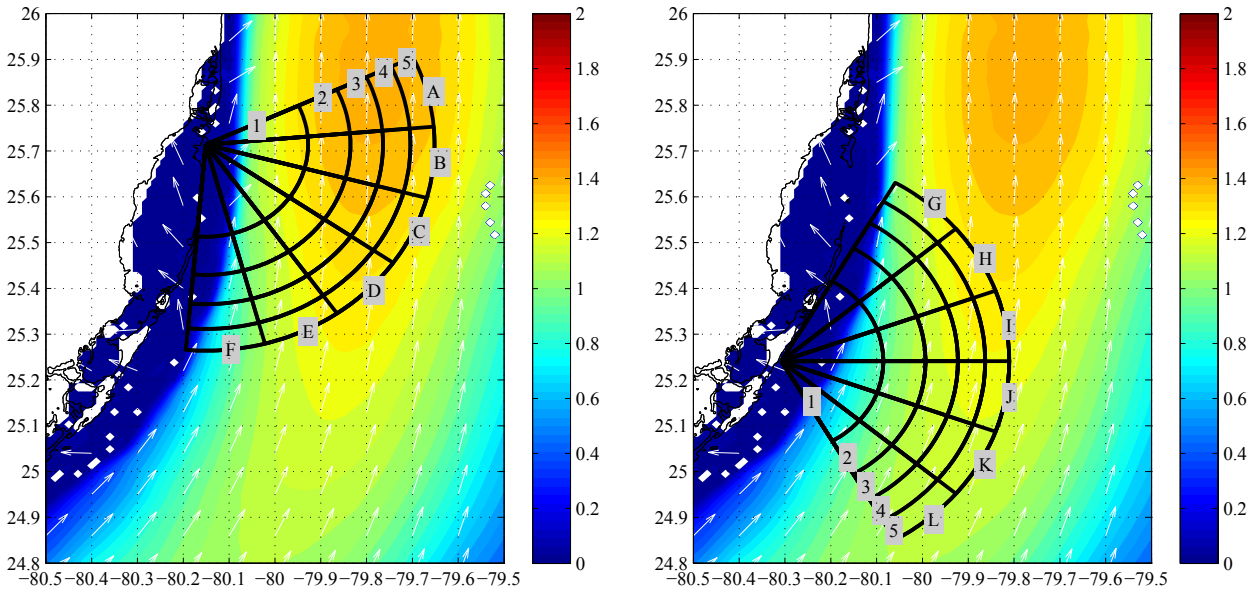

Figure 22 Radar sectors with example position of the Florida current (output from NCOM).

10 Model validation against radar

Time series comparisons of the radar data against co-located model output is given in Appendix A. An example plot from Appendix A is included here as Figure 23.

In these plots, one can see that the sign of wave height bias "control" vs "no currents" alternate from deep to shallow water in sectors E through L. Specifically, for the event on April 18, the " no currents" case (green line) is higher than "with currents" (blue line "control case") in shallow water. This reinforces what is observed in the in situ vs model comparisons. This behavior is not seen in sectors A-D, however.

Table 4 provides a summary of the error statistics from all of the plots in Appendix A, using the HF radar as ground truth. In several cases, the inclusion of currents results in a modest improvement to the correlation score and decrease in RMS error.

Figure 24 through Figure 26 show the same statistics in graphical form. One worrisome feature is that the skill of the model is generally better nearer the center of the bore-sight of the radar, section in D, E, J, and K having relatively high correlation values. This suggests that the model validation skill may have more to do with the quality (or lack thereof) of the observational data than the skill of the model to reproduce spatial variability of the real ocean in the *azimuthal position relative to the radar origin*. However, on a positive note, the comparisons such as shown in Figure 23 are actually quite good.

Another positive outcome from the comparison is that the spatial variability of the model in context of *range position relative to the radar origin*, roughly corresponding to water depth, *is* also observed in the radar. This is well-illustrated in Figure 27. Here, time-averaged waveheights are used, and we have normalized both the radar and model waveheight by their respective offshore values. The decrease in waveheight toward shore is clearly seen in both model and radar (i.e. excellent qualitative agreement).

Since this normalization is performed, we elected to use the non-calibrated radar "wave heights" in this comparison. Thus, this comparison is not sensitive to any uncertainty associated with calibration.

The radar observations also help us to understand the overprediction of *in situ* waveheights for the swell events (April 3, 17), as larger waves were measured offshore by the radar for these events. This supports the argument that the overprediction is caused by errors in swell propagation direction, rather than by a general overprediction of the swell energy. This highlights the advantage that radar provides to analyze spatially nonhomogeneous wave fields that are typical in the present case.

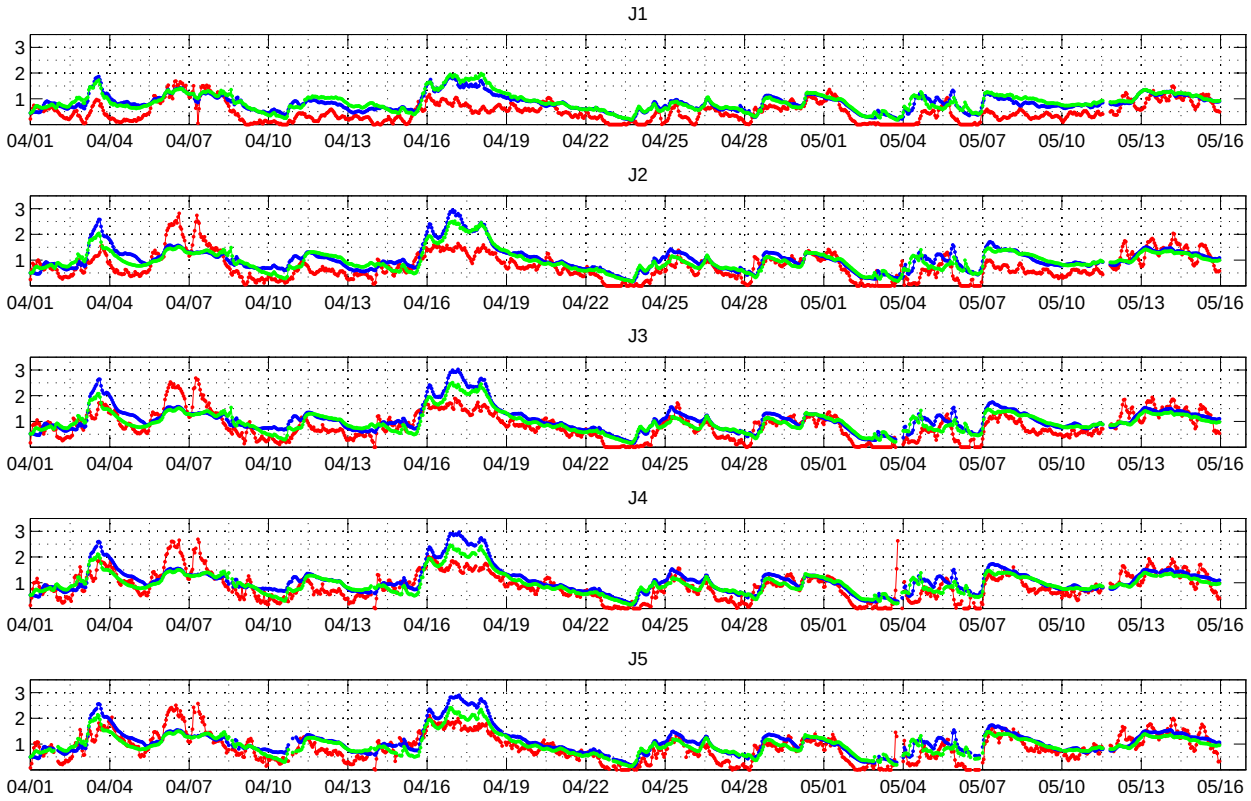

Figure 23. Example comparison of COAMPS (SWAN) fully coupled model output shown in blue vs. SWAN without currents (green) vs. calibrated radar (red). Significant waveheight, in meters.

CDN															
	1			2			3			4			5		
	bias	rmse	r	bias	rmse	r	bias	rmse	r	bias	rmse	r	bias	rmse	r
A	0.56	0.78	0.53	0.20	0.85	0.29	0.05	0.76	0.33	0.03	0.71	0.31	0.06	0.66	0.31
A_nc	0.48	0.65	0.51	0.06	0.76	0.24	-0.06	0.71	0.31	-0.06	0.67	0.29	-0.01	0.62	0.29
B	0.62	0.77	0.67	0.49	0.66	0.72	0.31	0.58	0.63	0.37	0.57	0.65	0.37	0.55	0.67
B_nc	0.52	0.64	0.64	0.36	0.52	0.67	0.19	0.50	0.57	0.26	0.47	0.63	0.28	0.47	0.65
C	0.57	0.77	0.47	0.45	0.63	0.70	0.32	0.51	0.73	0.35	0.52	0.73	0.33	0.50	0.73
C_nc	0.49	0.65	0.49	0.31	0.48	0.69	0.19	0.42	0.69	0.22	0.42	0.71	0.20	0.42	0.71
D	0.56	0.78	0.28	0.35	0.55	0.77	0.17	0.49	0.79	0.21	0.47	0.81	0.20	0.45	0.81
D_nc	0.53	0.73	0.29	0.22	0.51	0.73	0.05	0.52	0.74	0.08	0.48	0.77	0.08	0.46	0.77
E	0.49	0.62	0.36	0.27	0.54	0.71	-0.03	0.53	0.81	0.07	0.48	0.80	0.07	0.46	0.79
E_nc	0.54	0.68	0.31	0.22	0.56	0.64	-0.10	0.63	0.71	-0.02	0.55	0.72	-0.03	0.53	0.71
F	0.34	0.44	0.38	0.07	0.48	0.51	-0.25	0.62	0.55	-0.12	0.54	0.63	-0.08	0.46	0.70
F_nc	0.45	0.54	0.34	0.14	0.51	0.44	-0.21	0.64	0.45	-0.10	0.56	0.56	-0.08	0.49	0.63
NKL															
G	0.43	0.50	0.26	0.14	0.34	0.52	0.04	0.43	0.61	0.02	0.47	0.58	-0.01	0.47	0.67
G_nc	0.49	0.57	0.19	0.21	0.40	0.45	0.05	0.45	0.55	-0.03	0.51	0.46	-0.10	0.52	0.58
H	0.38	0.44	0.65	0.29	0.45	0.66	0.23	0.45	0.72	0.20	0.44	0.74	0.19	0.43	0.75
H_nc	0.45	0.51	0.61	0.29	0.46	0.60	0.15	0.41	0.66	0.09	0.39	0.70	0.08	0.39	0.71
I	0.37	0.46	0.64	0.34	0.51	0.65	0.30	0.49	0.68	0.27	0.48	0.70	0.27	0.46	0.72
I_nc	0.42	0.51	0.58	0.28	0.47	0.61	0.20	0.42	0.66	0.16	0.39	0.68	0.15	0.38	0.70
J	0.35	0.45	0.63	0.28	0.49	0.63	0.23	0.45	0.70	0.20	0.43	0.71	0.20	0.41	0.75
J_nc	0.38	0.49	0.59	0.22	0.45	0.63	0.13	0.39	0.70	0.09	0.37	0.72	0.08	0.35	0.75
K	0.29	0.45	0.60	0.22	0.48	0.57	0.16	0.43	0.64	0.11	0.40	0.68	0.09	0.40	0.69
K_nc	0.32	0.48	0.56	0.16	0.45	0.58	0.07	0.38	0.66	0.01	0.35	0.69	-0.01	0.35	0.71
L	0.28	0.46	0.57	0.16	0.52	0.46	0.04	0.50	0.47	-0.03	0.48	0.53	-0.05	0.46	0.56
L_nc	0.31	0.49	0.52	0.13	0.50	0.46	-0.02	0.48	0.49	-0.11	0.47	0.55	-0.14	0.45	0.58

Table 4: Statistics of model vs. WERA data sectors. Relatively good values are shown in green, and relatively poor values in red. Here, "nc" indicates the wave model simulations performed without surface currents as input. Skill is for significant waveheight, in meters. Statistics are calculated using the period 01-Apr-2005 00:00:00 to 15-May-2005 23:00:00.

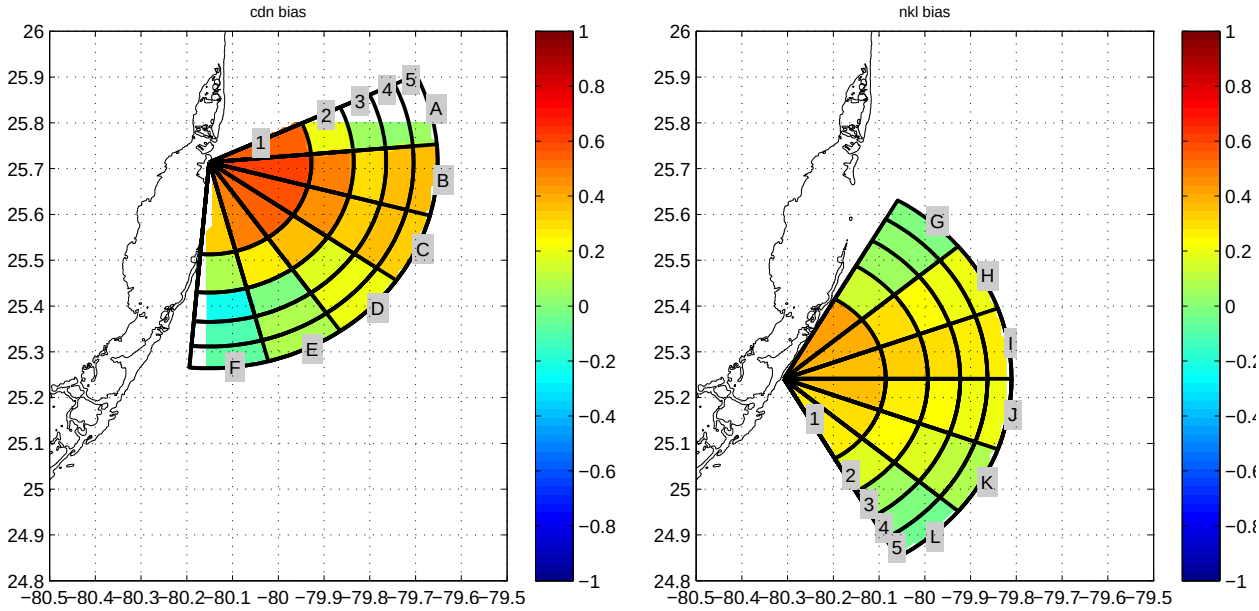

Figure 24 bias of significant waveheight, in meters.

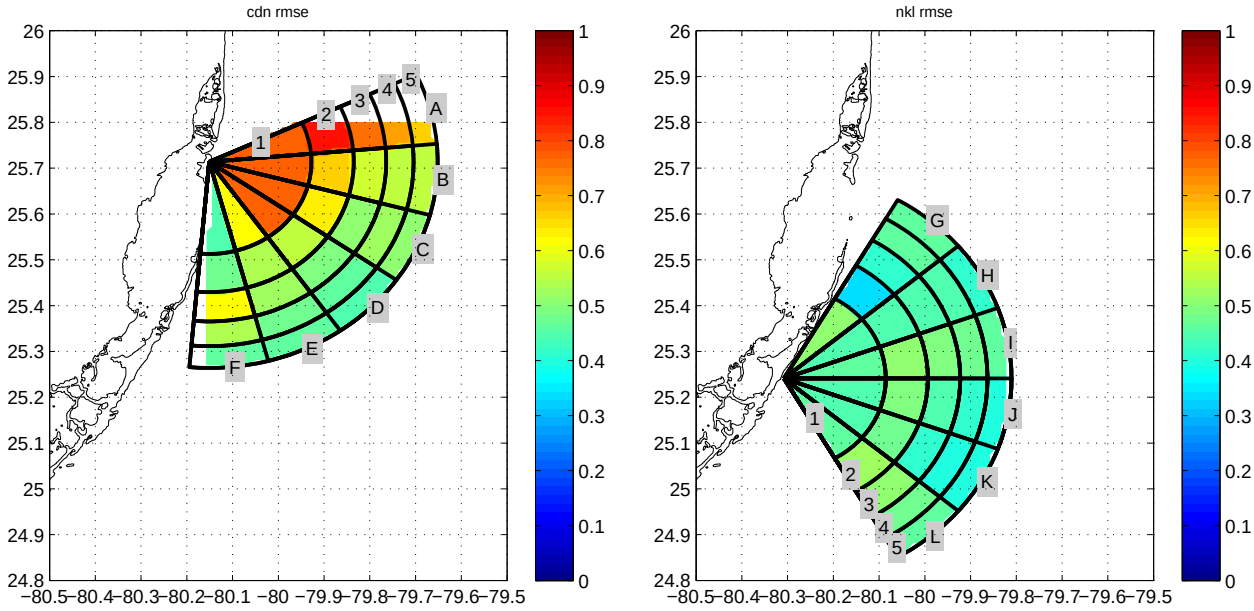

Figure 25 rms error of significant waveheight, in meters

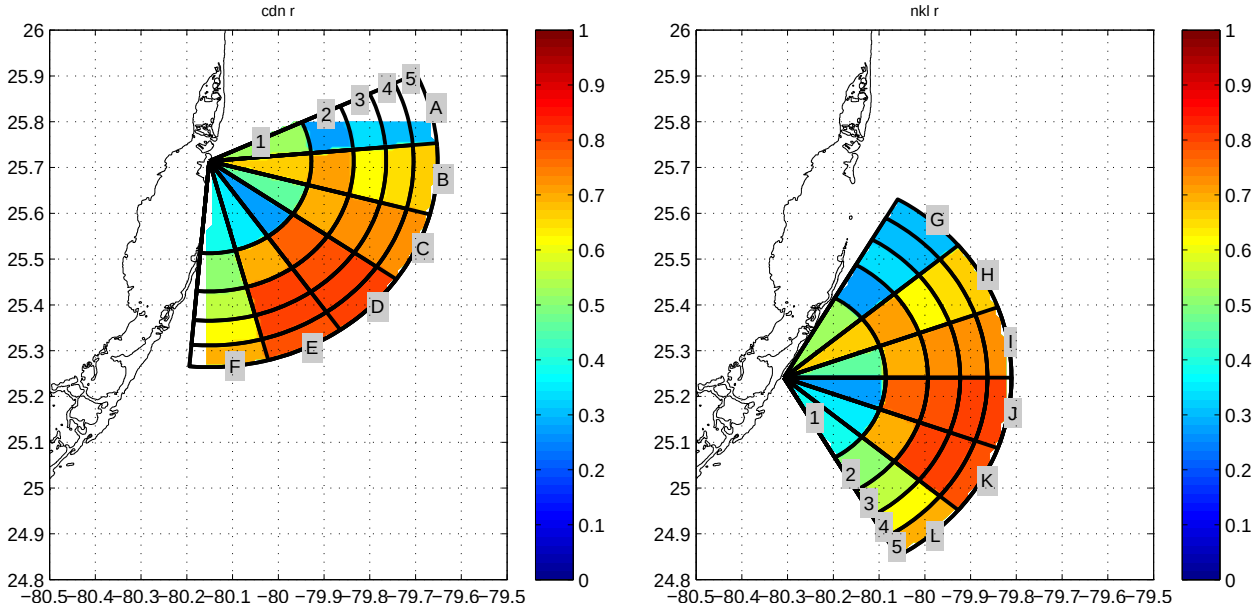

Figure 26. r statistic (correlation) for of significant waveheight

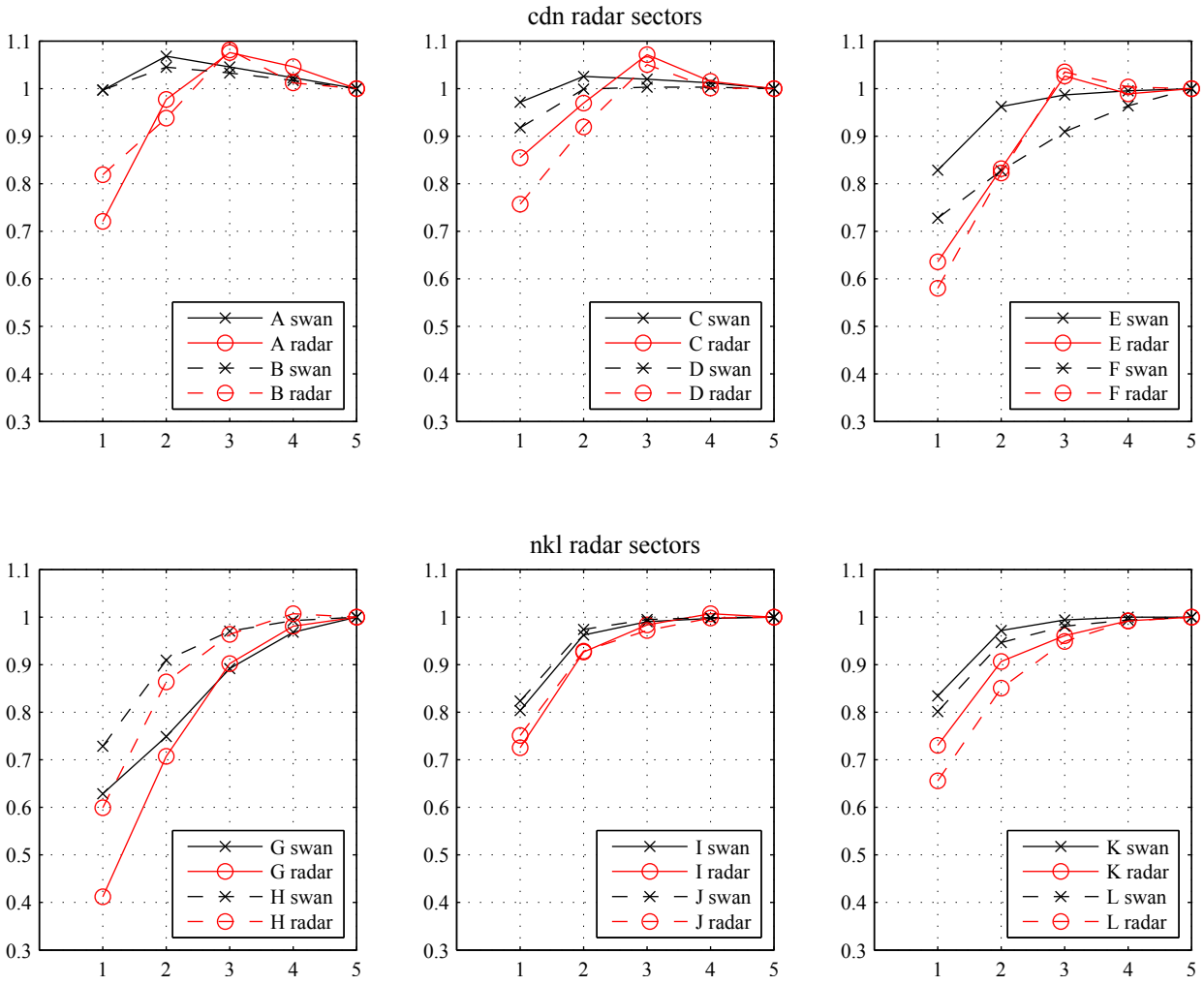

Figure 27 Normalized and time-averaged significant waveheights.

11 Summary

This document describes the wave model validation efforts for a Florida Straits test case for the fully coupled Coastal Ocean / Atmosphere Mesoscale Prediction System (COAMPS) model during spring of 2005. The "ground truth" for wave model validation includes in situ data (ADCP and buoy) and high frequency Wellen Radar (WERA HF) data collected by the University of Miami. The wave height comparison to in situ data is generally good, though some wave events are overpredicted by the model, most likely because of small, directional errors in the spectral boundary forcing. With regard to validation against the radar, the time series comparisons are mostly good. The wave model with surface current forcing has higher correlation with the radar than does the model without currents. This not only supports arguments for operational coupled modeling systems, but is also indirect evidence of wave-current interaction in the radar observations.

12 Acknowledgements

The WERA HF wave data was provided by Brian Huas of RSMAS and student (Gravois) involvement was made possible through the Naval Research Enterprise Internship Program.

13 References

Allard, R. A., T. J. Campbell, T. A. Smith, T. G. Jensen, J. A. Cummings, S. Chen, J. Doyle,X. Hong and R. J. Small, 2010: Validation Test Report for the Coupled Ocean/Atmosphere Mesoscale Prediction System (COAMPS) Version 5.0, *NRL Report* NRL/MR/7320--10-9283, 172pp.

Ardhuin, F. A., B. Chapron, and T. Elfouhaily, 2004: Waves and the air-sea momentum budget: implications for ocean circulation modeling, *J. Phys. Oceanogr.* **34**, 1741-1755.

Ardhuin, F. A., A. D. Jenkins, K. A. Belibassakis, 2008: Comments on "The Three-dimensional current and surface wave equations", *J. Phys. Oceanogr.* **38**, 1340-1350.

Booij, N., R.C. Ris, and L.H. Holthuijsen, 1999: A third-generation wave model for coastal regions, Part 1: Model description and validation. *J. Geophys. Res.* **104** (C4), 7649-7666.

Caires, S. I. N. 2000: *Comparative study of HF radar measurements and wave model hindcasts of waves in shallow waters*, PhD thesis, U. Sheffield, 355 pp.

Gurgel, K.W., G. Antonischki, H. Essen, T. Schlick, 1999: Wellen Radar (WERA): a new ground-wave HF radar for ocean remote sensing. *Coastal. Eng.* ,**37**(3-4), 219-234.

Grant, W.D. and O.S. Madsen, 1979: Combined wave and current interaction with a rough bottom, *J. Geophys. Res.*, **84**, 1797-1808

Haus, B. K., P. A. Work, G. Voulgaris, N. K. Shay, R. Ramos and J. Martinez , 2010: Wind speed dependence of single-site wave-height retrievals from high-frequency radars, *J. Atm. and Oceanic Techn.*, **27**, 1381-1394.

Haus, B.K., 2007: Surface current effects on the fetch limited growth of wave energy, *Journal of Geophysical Res.*, **112**, C03003, doi:10.1029/2006JC003924.

Hodur, R. M., 1997: The Naval Research Laboratory's Coupled Ocean/Atmospheric Mesoscale Prediction System (COAMPS). *Mon. Wea. Rev.*, **125**, 1414-1430.

Hogan, T.F. and Rosmond, T.E., 1991. The description of the U.S. Navy Operational Global Atmospheric Prediction System's spectral forecast models. *Mon. Wea. Rev.* **119**, 1786-1815.

Jensen, T. G., T. Campbell, T. A. Smith, R. J. Small and R. Allard, 2009: Cold air outbreak over the Kuroshio Extension Region, *MTS/IEEE Conference* Oceans 09, 4 pp.

Jensen, T. G., T. J. Campbell, R. A. Allard, R. J. Small and T. A. Smith, 2011: Turbulent heat fluxes during an intense cold-air outbreak over the Kuroshio Extension Region: results from a high-resolution coupled atmosphere-ocean model. *Ocean Dynamics* vol 61, 657-674, doi:10.1007/s10236-011-0380-0.

Longuet-Higgins, M.S. and R. W. Stewart, 1962: Radiation stresses and mass transport in surface gravity waves with application to ‘‘surf beats.’’ *J. Fluid Mech.,* **13,** 481–504.

Longuet-Higgins, M.S. and R.W. Stewart, 1964: Radiation stresses in water waves; a physical discussion, with applications, *Deep-Sea Res.*, **11**, 529-562.

Martin, P.J., 2000: *A Description of the Navy Coastal Ocean Model Version 1.0*. NRL Technical Report NRL/FR/7322-00-9962, 42 pp.

Ramos, R. H. C. Graber, B. K. Haus, 2009: Observation of wave energy evolution in coastal areas using HF radar. *J. Atm. and Oceanic Techn.*, **26**, 1891-1909.

Rogers, W.E., J.M. Kaihatu, L. Hsu, R.E. Jensen, J.D. Dykes, K.T. Holland, 2007: Forecasting and hindcasting waves with the SWAN model in the Southern California Bight. *Coastal Eng.* **54**, 1-15.

Shay, L. K. J. Martinez-Pedraja, T.M. Cook, and B.K. Haus, 2007: High-frequency radar mapping of surface currents using WERA. *J. Atm. Oceanic. Tech.*, **24**, 484-503.

Shay, L. K. H. Seim, D. Savidge, R. Styles, R. H. Weisberg, 2008: High frequency radar observing systems in SEACOOS: 2002-2007 lessons learned, *Marine Technology Society Journal,* **42**(3), 55-670.

Smith, T. A., T. Campbell, R. J. Small and R. Allard, 2009: Two-Way Atmospheric and Oceanic Coupling of the Adriatic Bora, *MTS/IEEE Conference* Oceans '09, 11 pp.

Smith, T. A., T. J. Campbell, R. A. Allard and S. N. Carroll, 2010: User's Guide for the Coupled Ocean/Atmospheric Mesoscale Prediction System (COAMPS) Version 5.0, *NRL Report* NRL/MR/7320--10-9208, 83 pp.

Small, R. J., T. Campbell, J. Teixeira, S. Carniel, T. A. Smith, J. Dykes, S. Chen and R. Allard, 2011: Air-Sea Interaction in the Liguarian Sea: Assessment of a Coupled Ocean-Atmosphere Model Using In Situ Data from LASIE07, Monthly Weather Review, **139**, 1785-1808, doi:10.1175/2010MWR3431.1.

SWAN team, 2010: SWAN Scientific and Technical Documentation, SWAN Cycle III version 40.81, Delft University of Technology, http://www.swan.tudelft.nl , 118 pp.

Tang, C. L., W. Perrie, A. D. Jenkins, B. M. DeTracey, Y. Hu, B. Toulany, and P. C. Smith, 2007: Observation and modeling of surface currents on the Grand Banks: A study of the wave effects on surface currents, *J. Geophys. Res.*, **112**, C10025, doi:10.1029/2006JC004028.

Tolman, H.L, 2009: User Manual and System Documentation of WAVEWATCH III^{TM} Version 3.14, Tech. Note, NOAA/NWS/NCEP/MMAB, 220 pp.

Voulgaris, G., Haus, B. K., P. Work, L. K. Shay, H. Seim, R. H. Weisberg and J. R. Nelson, 2008: Waves initiative within SEACOOS, *Marine Technology Society Journal*, **42**(3), 68-80.

Wyatt, L. R., S. P. Thompson, and R. R. Burton, 1999: Evaluation of high frequency radar wave measurement. *Coastal Eng.*, **37**, 259-282.

Wyatt, L. R., and Coauthors, 2003: Validation and intercomparisons of wave measurements and models during the EuroROSE experiments. *Coastal Eng.*, **48**, 1-28.

14 Appendix A: Time series plots by sector

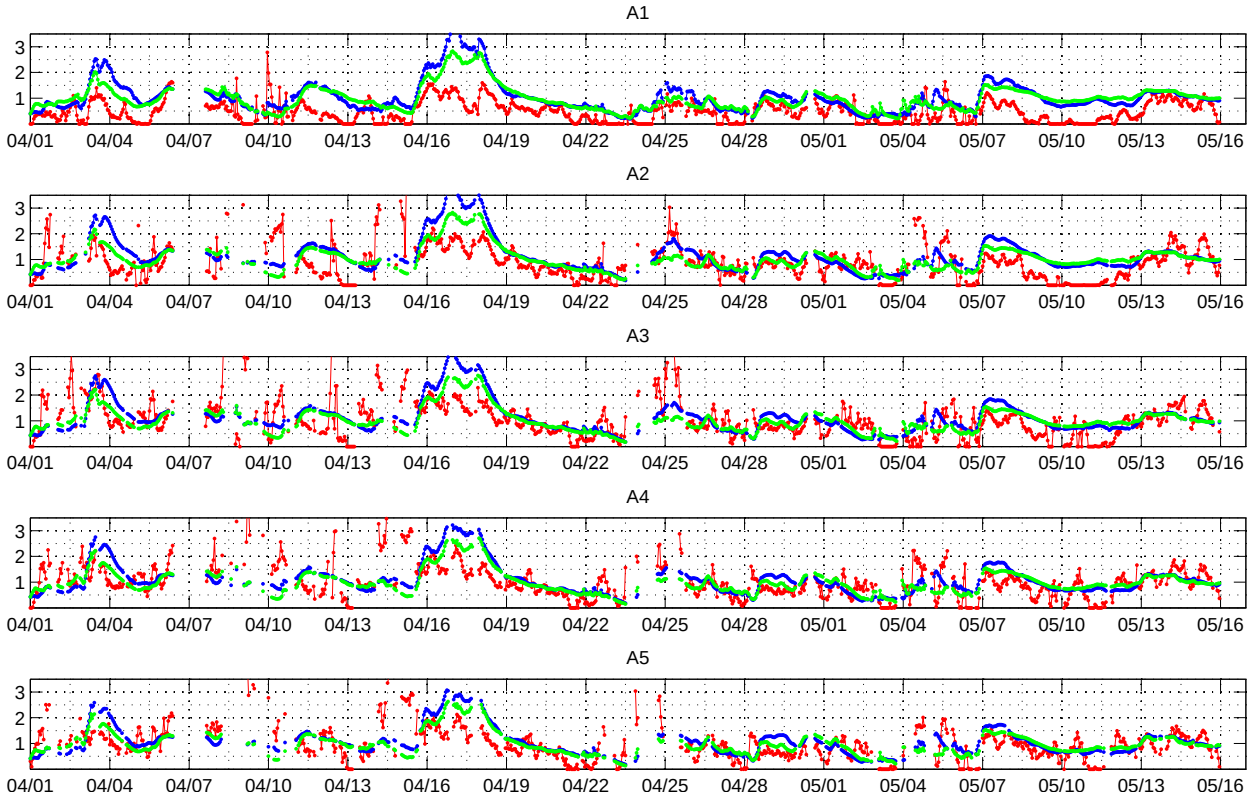

Figure 28. Comparison of COAMPS (SWAN) fully coupled model output shown in blue vs. SWAN without currents (green) vs. calibrated radar (red).

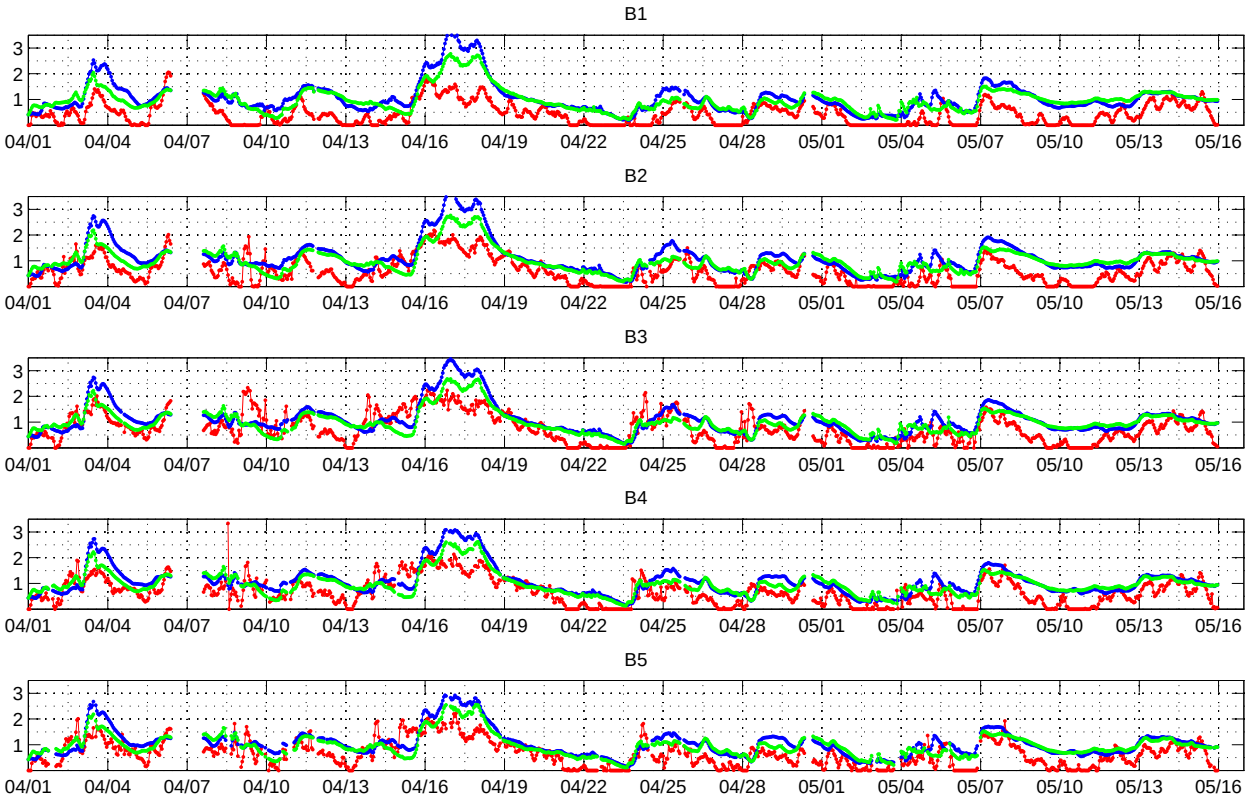

Figure 29. Similar to Figure 28, except for different sectors, as indicated in the plot titles.

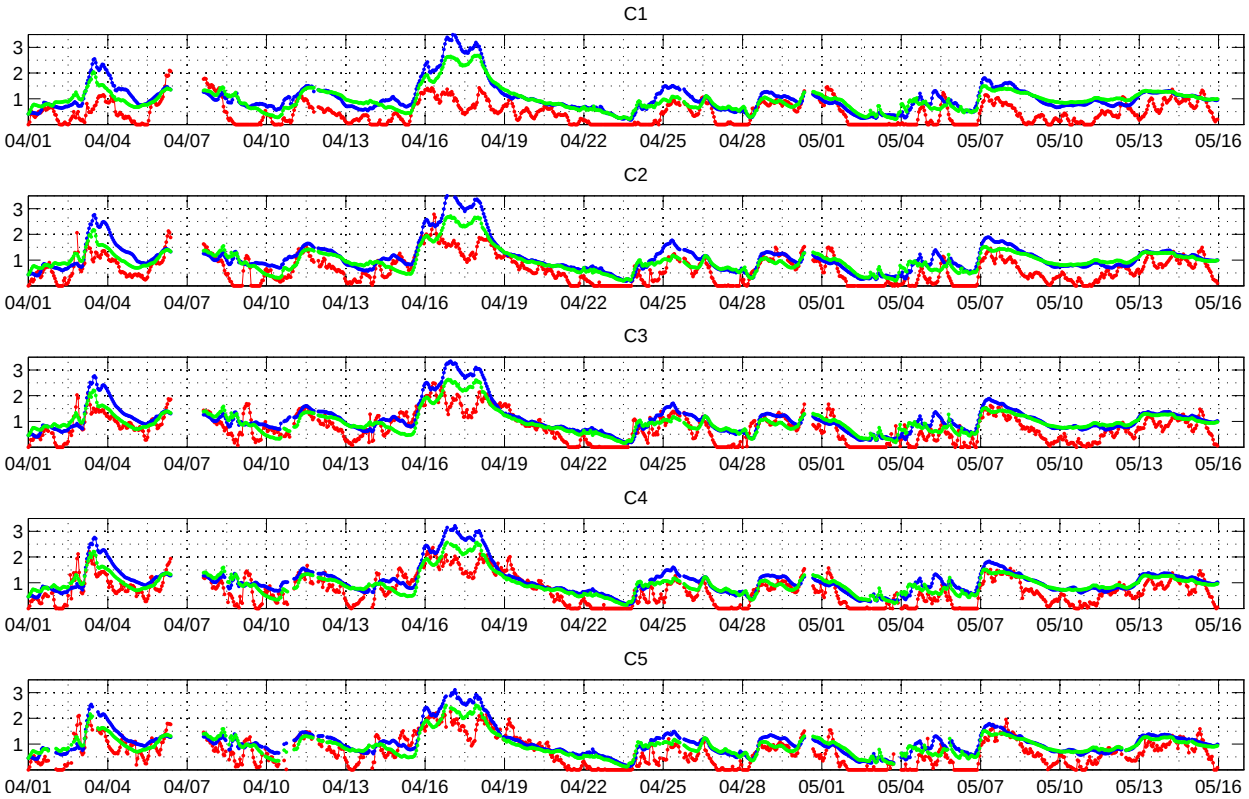

Figure 30. Similar to Figure 28, except for different sectors, as indicated in the plot titles.

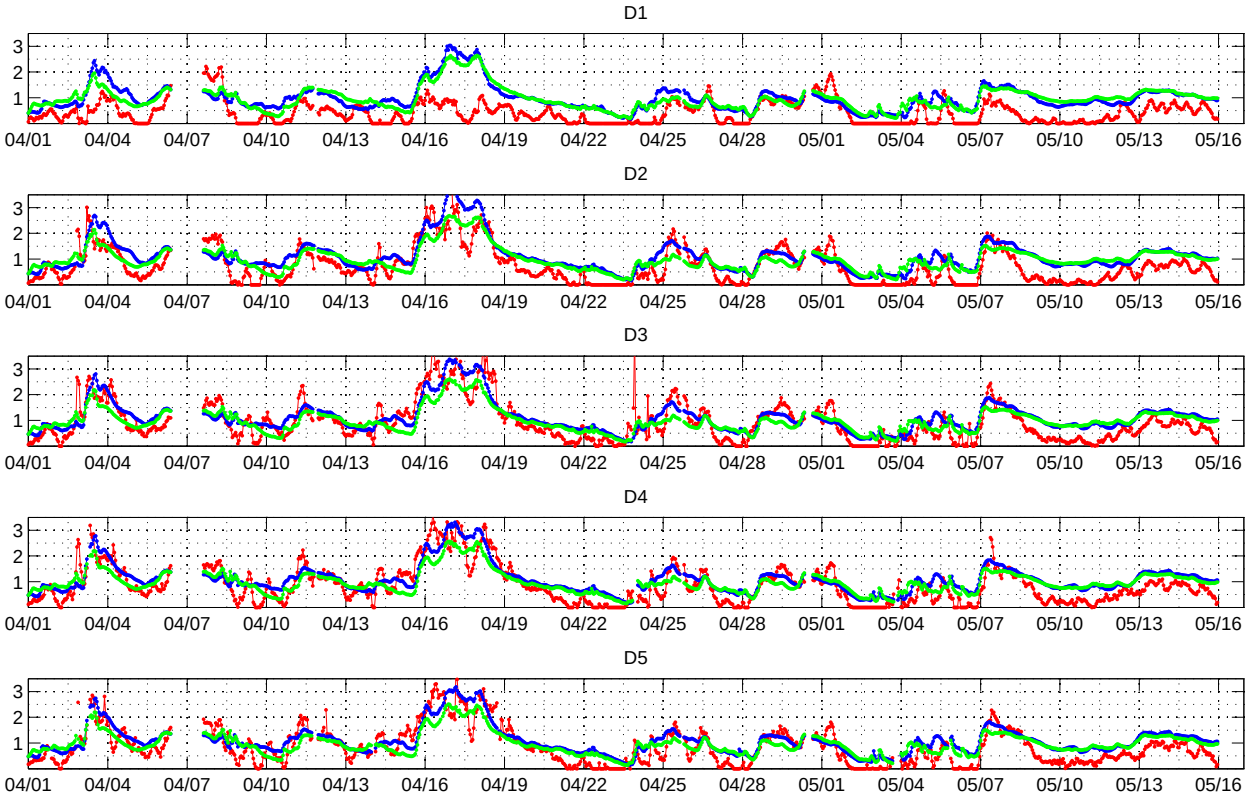

Figure 31. Similar to Figure 28, except for different sectors, as indicated in the plot titles.

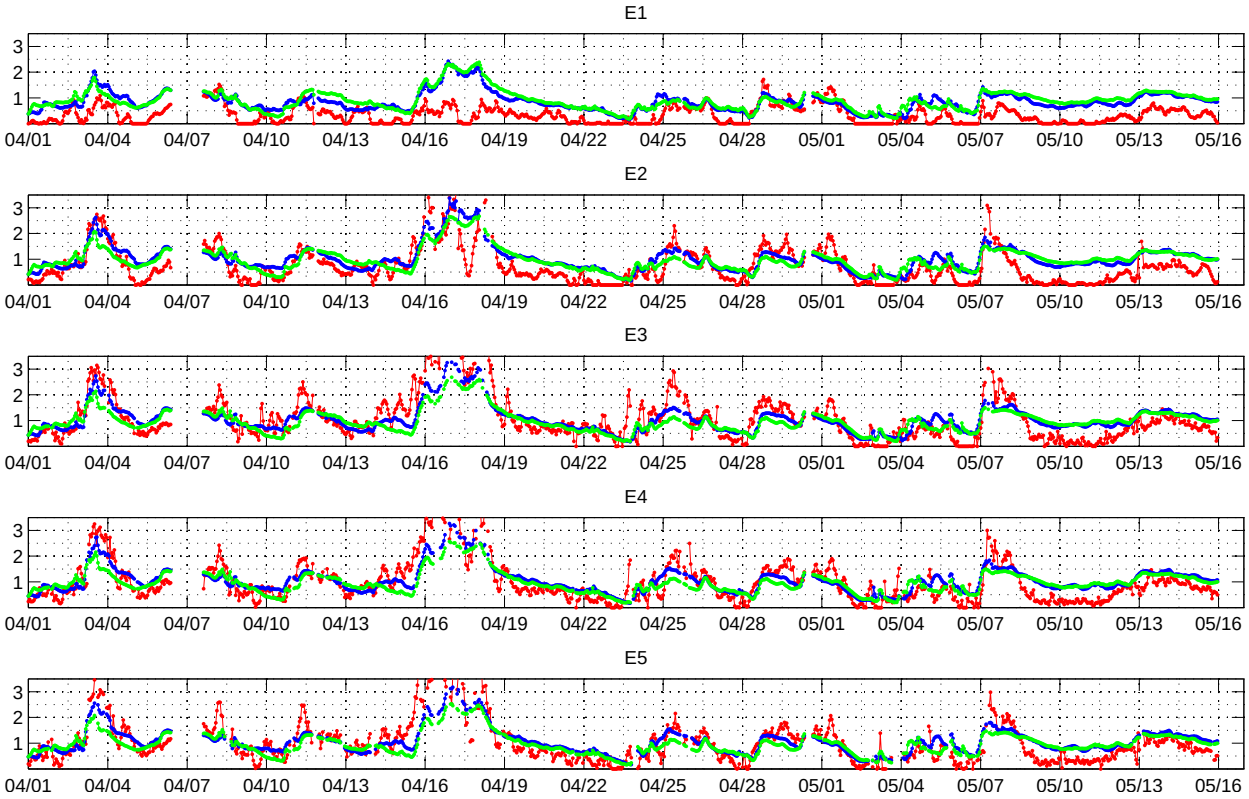

Figure 32. Similar to Figure 28, except for different sectors, as indicated in the plot titles.

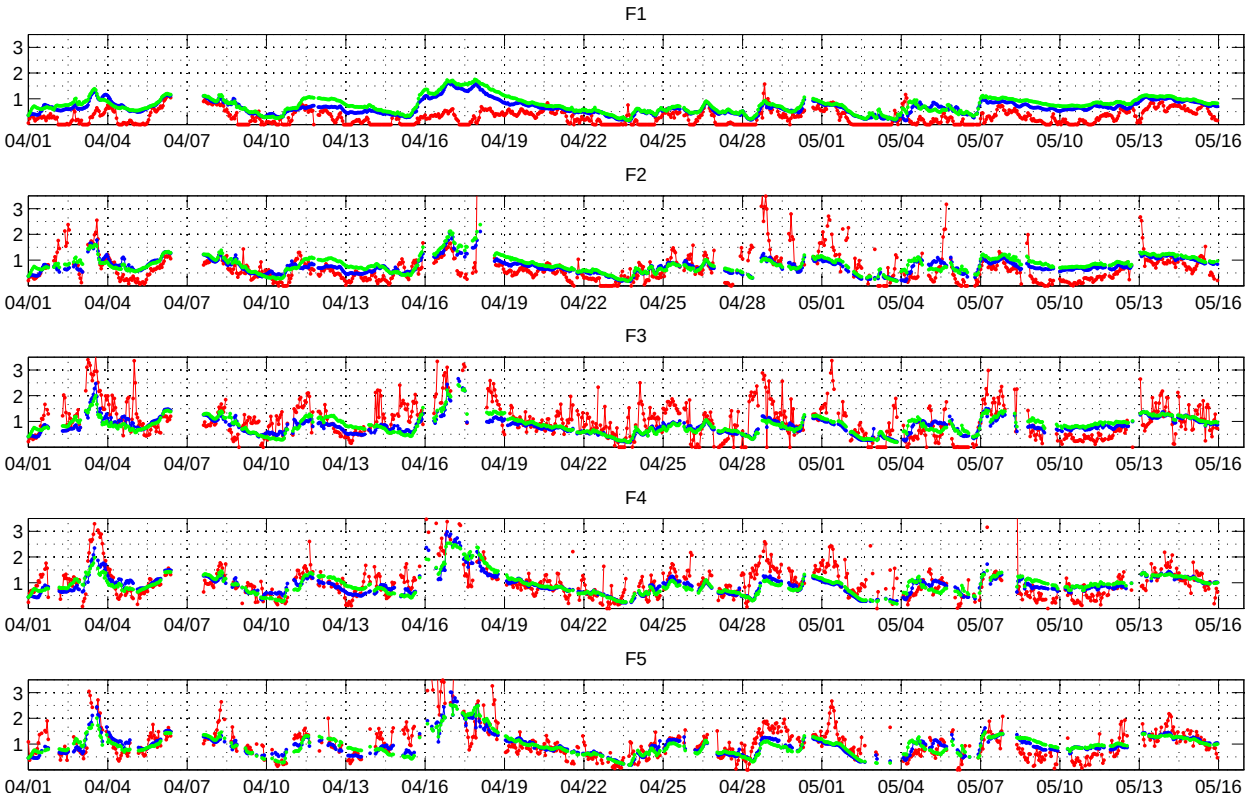

Figure 33. Similar to Figure 28, except for different sectors, as indicated in the plot titles.

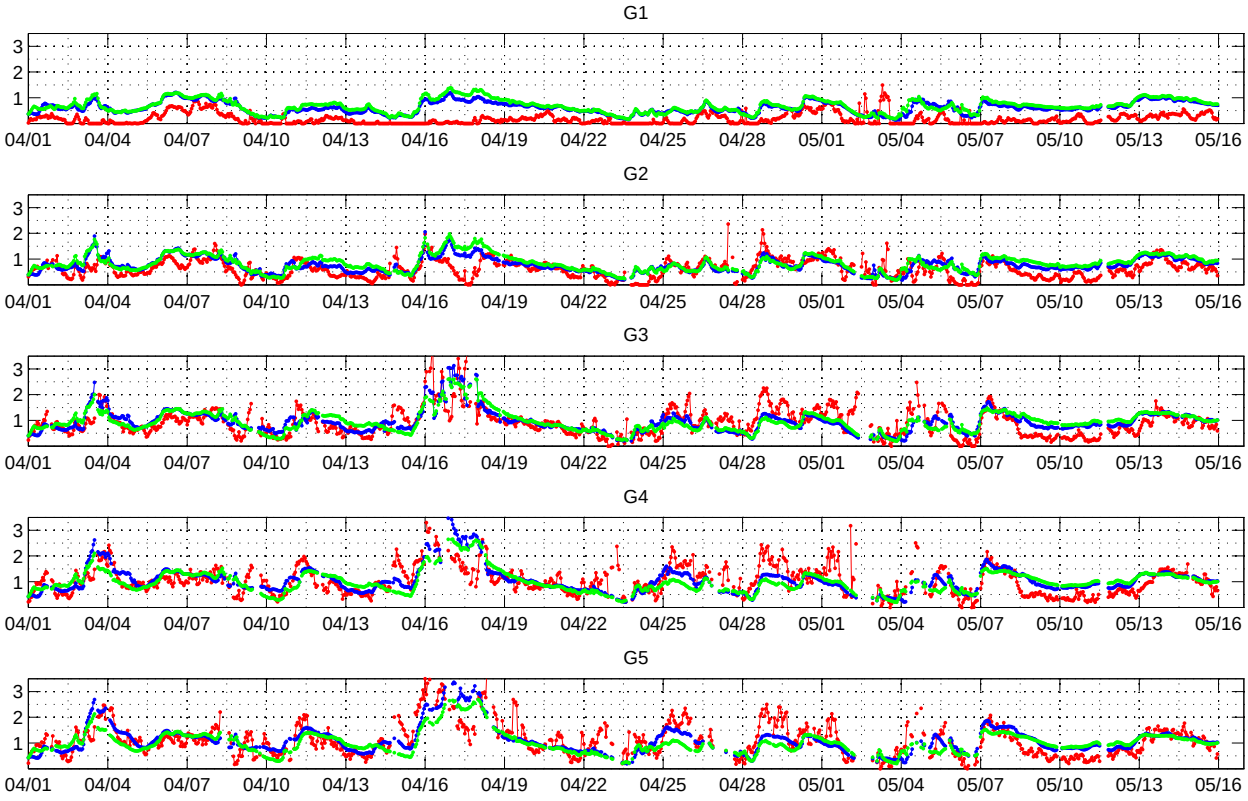

Figure 34. Similar to Figure 28, except for different sectors, as indicated in the plot titles.

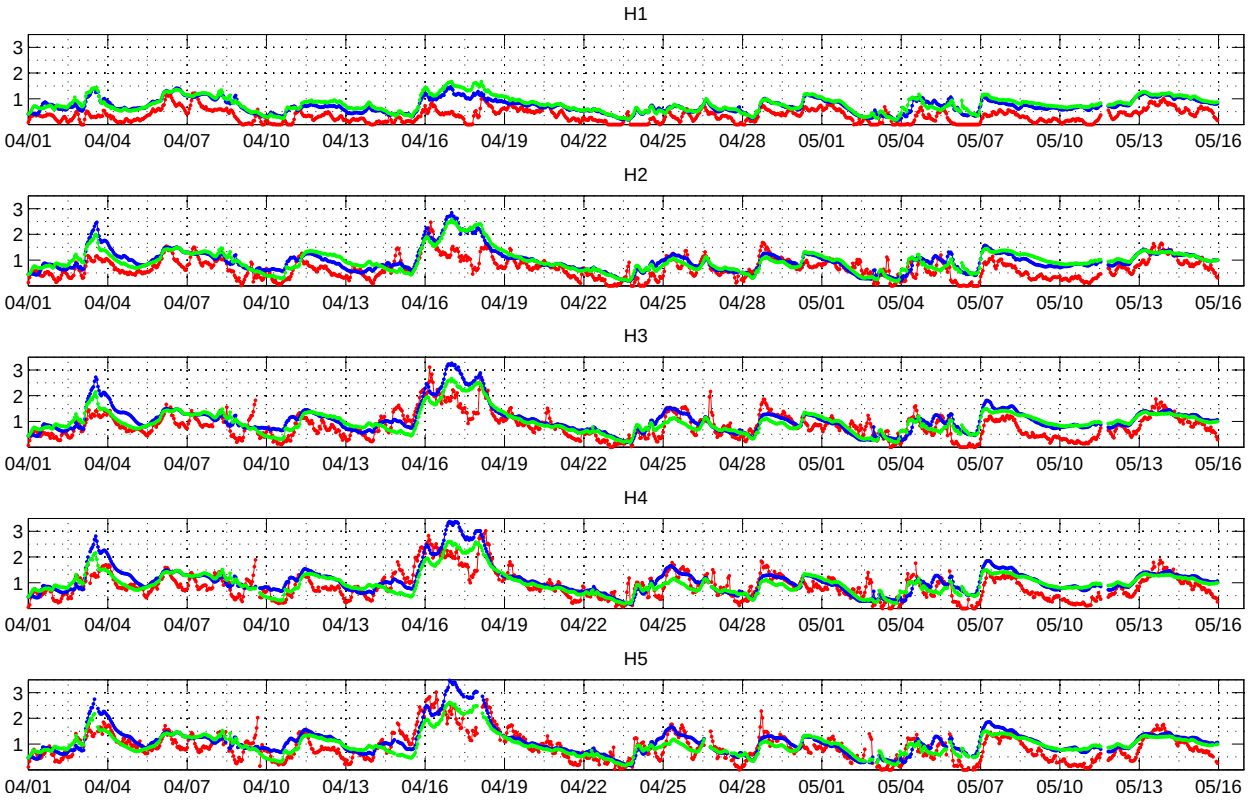

Figure 35. Similar to Figure 28, except for different sectors, as indicated in the plot titles.

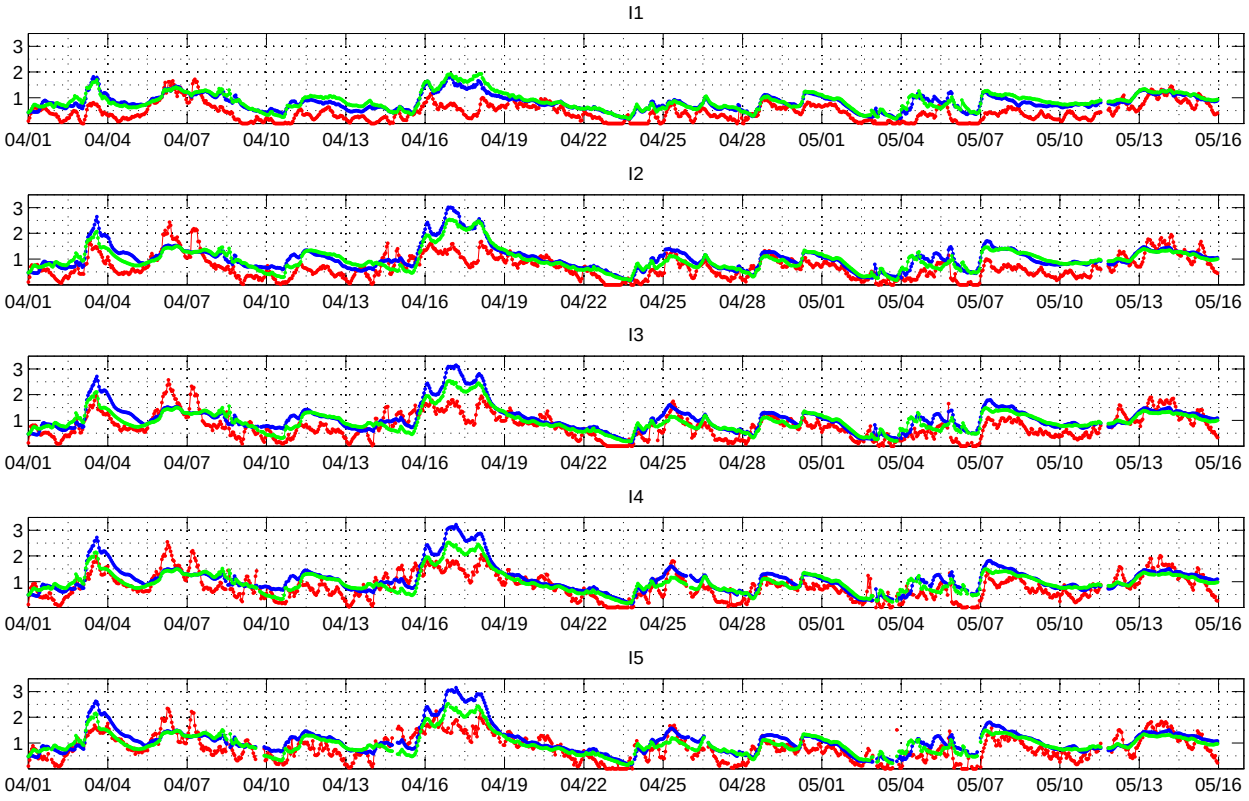

Figure 36. Similar to Figure 28, except for different sectors, as indicated in the plot titles.

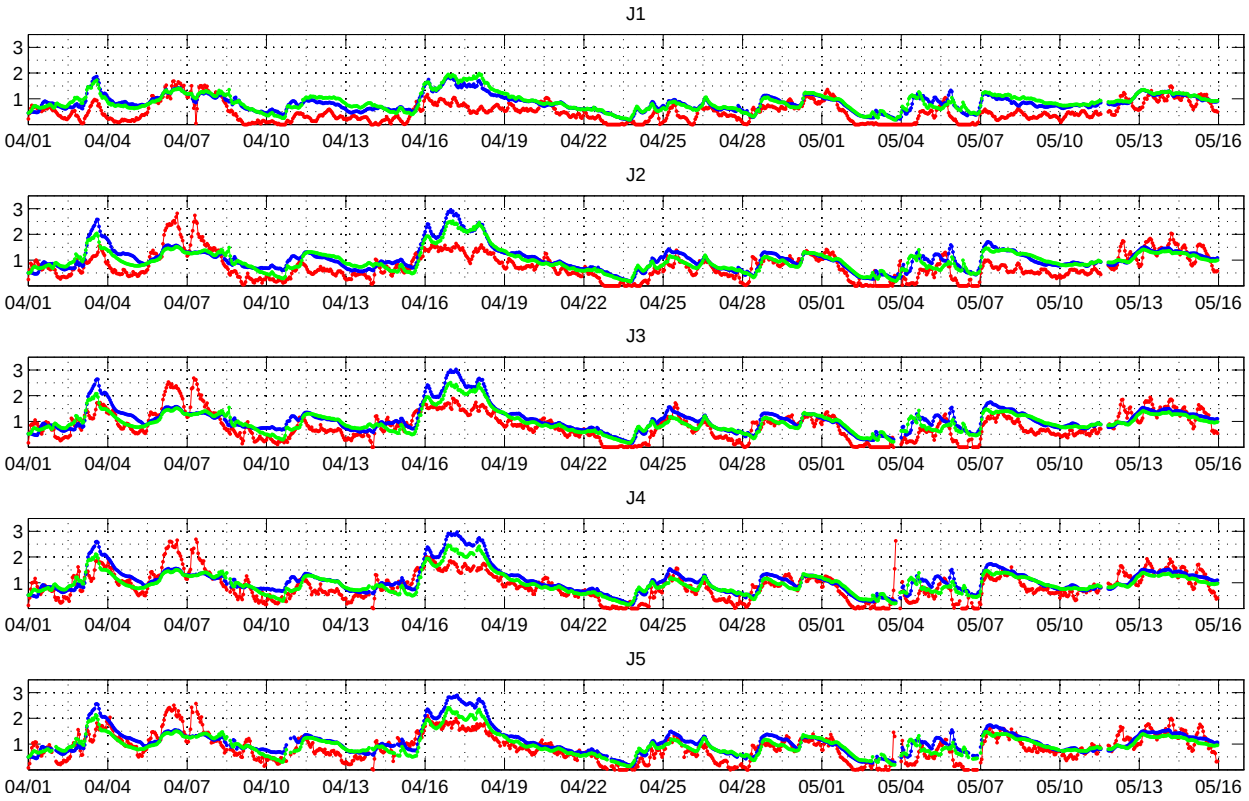

Figure 37. Similar to Figure 28, except for different sectors, as indicated in the plot titles.

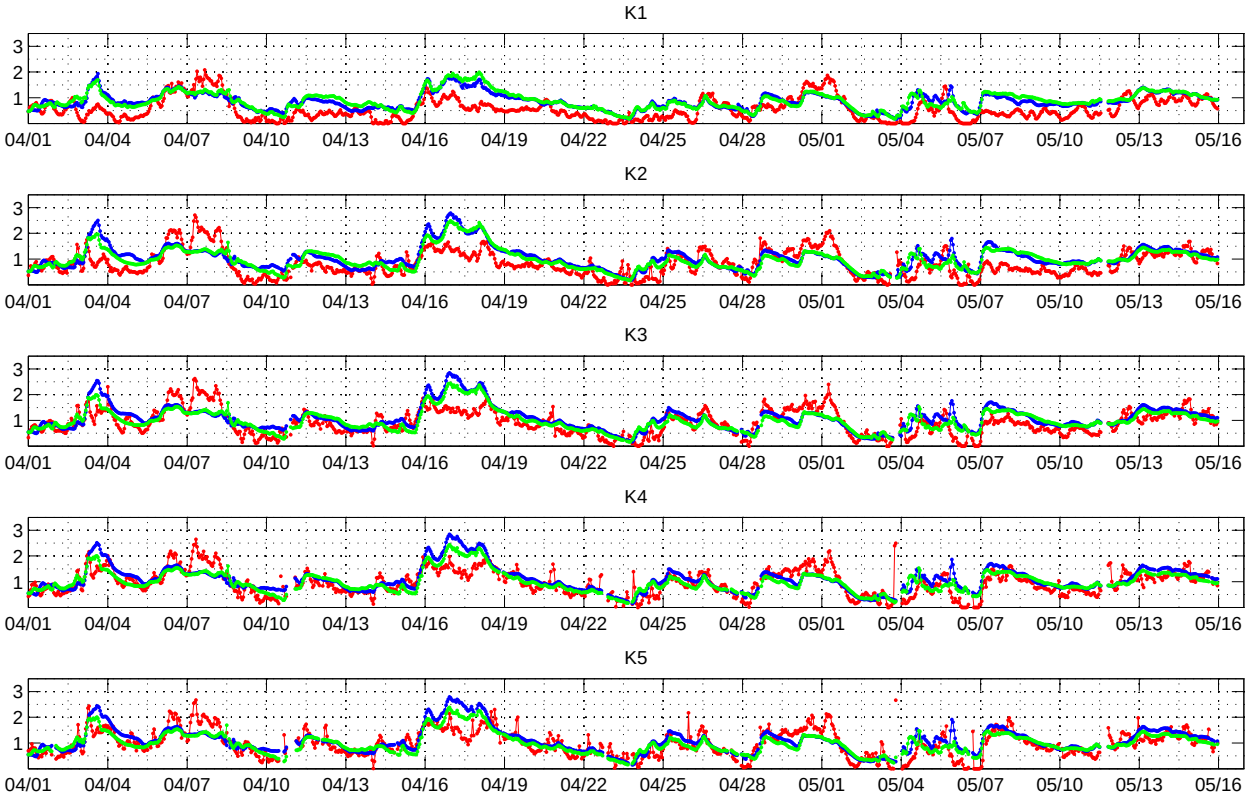

Figure 38. Similar to Figure 28, except for different sectors, as indicated in the plot titles.

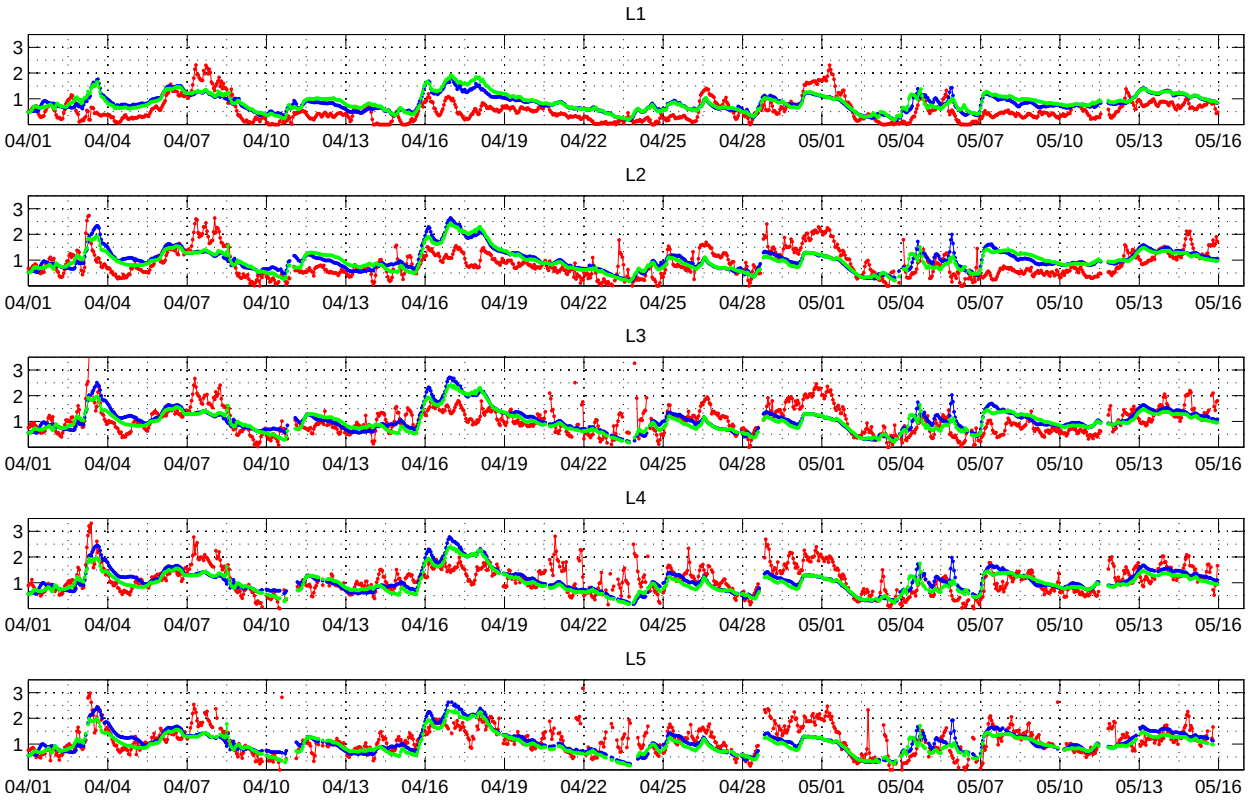

Figure 39. Similar to Figure 28, except for different sectors, as indicated in the plot titles.